A comprehensive experimental characterization of the iPIX gamma imager

Published by IOP Publishing for Sissa Medialab

Received: *May 9, 2016*
Revised: *July 19, 2016*
Accepted: *July 29, 2016*
Published: *August 16, 2016*

2016 JINST 11 P08012

A comprehensive experimental characterization of the iPIX gamma imager

K. Amgarou,[a,1] **V. Paradiso,**[a,b,2] **A. Patoz,**[a] **F. Bonnet,**[a] **J. Handley,**[a,b] **P. Couturier,**[a] **F. Becker**[c] **and N. Menaa**[a]

[a] *CANBERRA Industries Inc.,*
1, rue des Hérons, Saint Quentin en Yvelines, F-78182 France
[b] *CERN, Experimental Physics Department, ATLAS Detector Operation,*
Geneva 23, CH-1211 Switzerland
[c] *Karlsruhe Institute of Technology — KIT, Institute for Nuclear Waste Disposal,*
Hermann-von-Helmholtz-Platz 1, Eggenstein-Leopoldshafen, 76344 Germany

E-mail: vincenzo.paradiso@canberra.com

Abstract: The results of more than 280 different experiments aimed at exploring the main features and performances of a newly developed gamma imager, called iPIX, are summarized in this paper. iPIX is designed to quickly localize radioactive sources while estimating the ambient dose equivalent rate at the measurement point. It integrates a 1 mm thick CdTe detector directly bump-bonded to a Timepix chip, a tungsten coded-aperture mask, and a mini RGB camera. It also represents a major technological breakthrough in terms of lightness, compactness, usability, response sensitivity, and angular resolution. As an example of its key strengths, an ^{241}Am source with a dose rate of only few nSv/h can be localized in less than one minute.

Keywords: Dosimetry concepts and apparatus; Search for radioactive and fissile materials

[1] Present address: CEA, DEN/MAR/DPAD/CMET, B.P. 17171, Bagnols sur Cèze, F-30207 France.
[2] Corresponding author.

doi:10.1088/1748-0221/11/08/P08012

Contents

1 Introduction

In-situ localization of radiation emitting objects or hotspots is of prime concern during decommissioning and clean-up activities of nuclear facilities at the end of their life-cycle. It is also of great importance in homeland security for detecting illicit traffic of nuclear materials as well as in crisis managements of radiological emergency situations for recovering orphan or lost radioactive sources on the one side, and for delimiting suspicious radiological contaminated areas after an accident event or malevolent act on the other side [1–3].

Gamma imaging technique, applied for the first time by Anger in 1952 as a human body tomographic scanner to detect early stage tumours [4], provides an optimal solution to track X- or γ-ray emitting objects from greater distances than conventional rate meters, thus significantly reducing the radiation dose received by operators in line with the well-known ALARA principle. However, the associated equipment usually used for medical applications is generally too bulky, heavy, and complex to be employed for in-field monitoring.

2016 JINST 11 P08012

An earlier attempt to develop a portable gamma imager was carried out in the 1990s by CEA. The outcome of this effort was the CARTOGAM instrument [5], which has been widely commercialized by CANBERRA during the last decade. This instrument is a mature technology combining an inverted double-cone collimator (i.e., two right circular cones placed apex-to-apex) to be used as a single pinhole aperture, a CsI/Tl (thallium doped caesium iodide) scintillation crystal, a multi-channel image intensifier, and a CCD camera. With the exception of the pinhole aperture, the whole instrument is fully shielded against background radiation.

CARTOGAM applies the same approach of a basic photographic camera (i.e., a light-opaque box with a pinhole aperture through which the light coming from an object is projected inside to form an inverted image). Although it is still demonstrating good performances, namely at severe irradiation conditions, its heavy weight (~18 kg) poses several constraints from a practical point of view. In addition, its detection efficiency is quite limited by the small size of its pinhole aperture.

To overcome these shortcomings, CANBERRA has recently developed a second-generation gamma imager, called iPIX (figure 1), in the framework of a partnership agreement with CEA [6–8]. iPIX integrates a 1 mm thick CdTe (cadmium telluride) detector directly bump-bonded to a Timepix chip [9], a tungsten coded-aperture mask (i.e., a front-end collimator with several pinholes) [10], and a mini RGB camera. Under this configuration, the real view of the scene under study is firstly taken by the mini RGB camera and is subsequently superimposed by the associated X- or γ-ray information (i.e., a sort of color map display) derived as a result of the mask pattern design (see section 2.2 for more details).

The coded-aperture technique has played a crucial role in astronomy to help resolving the origin of γ-ray bursts from distant galaxies [11] and can be used under a mask/anti-mask mode [12] to reduce the background noise interference without the need of heavy radiation shielding. This allows for an ultra-portable (2.35 kg) and compact ($9 \times 9 \times 18.8$ cm^3) device, which is remotely controlled (via a single Ethernet cable up to 80 meters long) by means of an easy-to-use, fully ergonomic, and highly intuitive Graphical User Interface (GUI). The latter when launched is systematically configured and, with only one click, a new acquisition can be started.

Other main features of iPIX are:

- Easily deployable and plug-and-play system,
- Automatic parameter settings,
- Dynamic display of the measurement progress,
- Industrial design for use in harsh environments,
- Dust and water proof,
- Easy to clean, especially for unwanted radioactive contamination,
- Protection against unpredictable vibrations, chocks and falls,
- More than five hours autonomy, and
- Motorized pan-tilt support.

2016 JINST 11 P08012

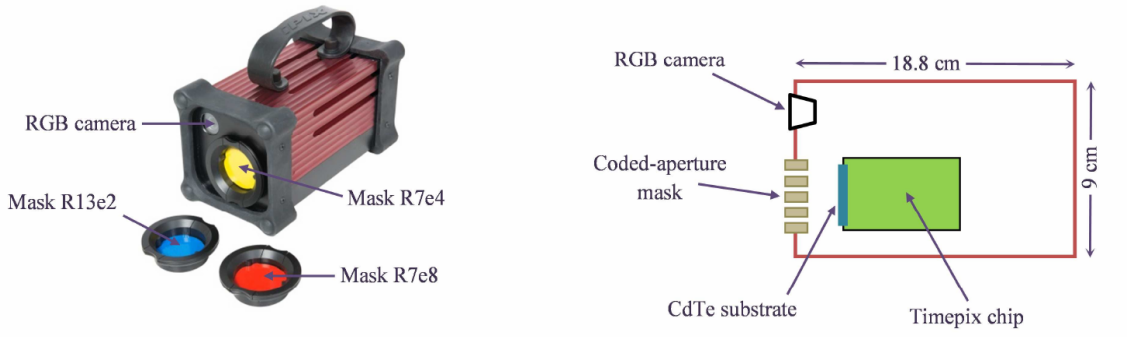

Figure 1. The iPIX gamma imager (left) together with a cross-section not to scale (right) showing its mains components and relevant dimensions. It has three coded-aperture masks (see section 2.2) that are labelled by different colors to facilitate their identification during measurements.

The present paper is mainly focused on the description of the iPIX gamma imager. It also analyzes and discusses the results of a comprehensive experimental study, carried out with ISO narrow X-ray beams or N-Series [13] and standard radioactive sources.

2 Materials and methods

2.1 Timepix chip

The Timepix chip is a pixelated CMOS ASIC directly bump-bounded to a given semiconductor substrate in order to detect X- or γ-rays (hereafter referred to as "photons"). It consists of 256 $\times$ 256 square pixels with 55 μm side, providing a global detection area of 14 $\times$ 14 mm^2. Each pixel contains ~550 transistors with ~13.5 μW static power consumption and it has its own electronic circuitry: charge-sensitive amplifier, discriminator with polarity control pin, 4-bit DAC offset for threshold adjustment, synchronization logic, 8-bit configuration register, and 14-bit counter.

The photon detection is based on a depletion region that is formed in the vicinity of the PN junction under a reverse-bias voltage. The number of collected charge carriers (electrons and holes) is expected to be proportional to the amount of the energy deposited in the depletion region by the passage of ionizing radiation. However, the active pixels give no signal when the pre-set threshold level (THL) is not crossed. The 14-bit counter of each pixel operates only when the Timepix shutter is open (see section 2.1.1) and has an overflow control that stops at 11810 counts [9]. All the Timepix parameters are easily configured via Pixelman, a cross-platform and modular software tool developed by the Czech Technical University in Prague [14].

Figure 2 compares the energy dependence of photon absorption probability, which is directly related to the photon detection efficiency, for the three substrates (Si, CdTe and GaAs) that can be currently chosen for the Timepix chip. According to this figure, CdTe has globally a better photon absorption probability due to its high atomic number and density (Z = 48.52 and ρ = 5.32 g cm^{-3}). The maximum difference, up to a factor 20 around 50–70 keV, is shown between CdTe and Si. At this energy range, the photon absorption probability on CdTe is near 50%. However, the three materials provide quite comparable behaviour at photon energies above 400 keV showing low absorption probabilities (<1%).

2016 JINST 11 P08012

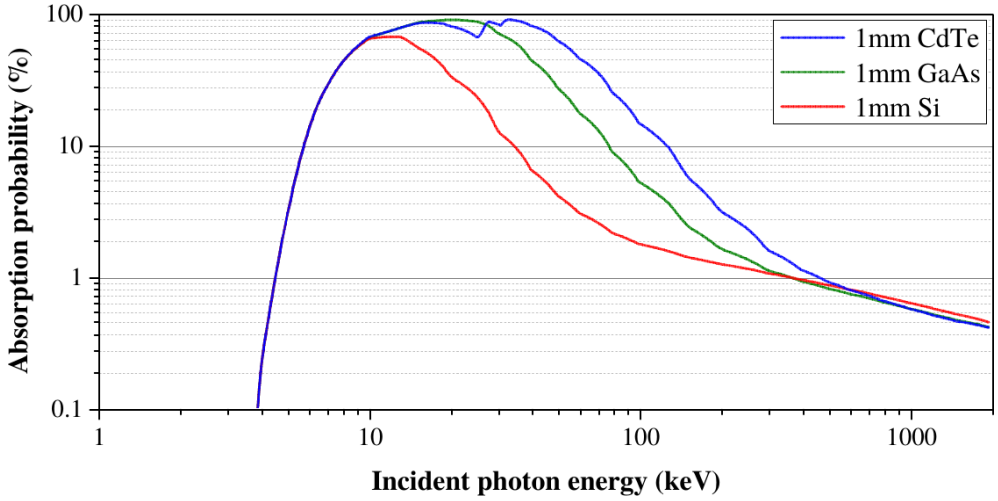

Figure 2. Absorption probability for CdTe, GaAs and Si as a function of incident photon energy.

2.1.1 Counting modes

Every pixel of the Timepix chip can be independently configured to run in one of the following four different operating modes:

- Masked mode: individual pixels can be masked.
- Medipix (MPX) mode: the pixel counter is incremented by one each time its output signal crosses the pre-set threshold level.
- Time-over-Threshold (ToT) or energy mode: the counter is incremented continuously as long as the pixel output signal is above the pre-set threshold level. The number of clock cycles is counted until the pixel output signal crosses back below this threshold. As stated in section 2.1.3, the number of clock cycles can be directly related to the voltage amplitude of the pixel output signal.
- Time-of-Arrival (ToA) or time mode: the counter is incremented continuously from the time the pixel output signal crosses the pre-set threshold level until the closure of the shutter. This mode is beyond the iPIX scope and will not be addressed hereafter since it is essentially used in the Large Hadron Collider (LHC) at CERN for accurate tracking of fundamental particles [15].

A reference clock with up to 100 MHz frequency is used for the last two counting modes. However, as the iPIX default clock frequency is fixed to 9.6 MHz, each ToT unit corresponds to a time period of 1.042×10^{-7} sec.

As pointed out before, all the above counting modes rely on the configured shutter-time, which is the active time during which the Timepix sensor is kept switched on. When this shutter-time ends, pixel values are retrieved from the buffer and cleared. The process repeats for the duration of the measurement (i.e., until the chosen number of frames is reached). A comparison between MPX and ToT modes is illustrated in figure 3.

2016 JINST 11 P08012

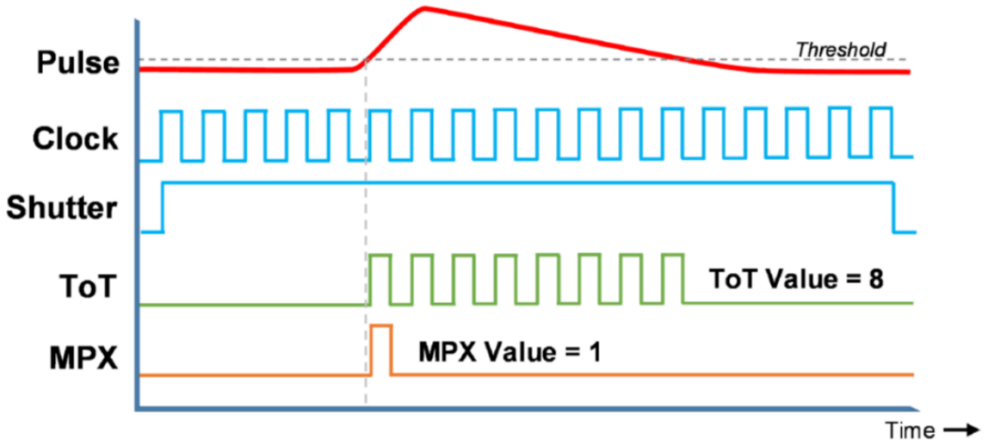

Figure 3. Comparison between MPX and ToT modes of the Timepix chip.

2.1.2 Charge sharing between adjacent pixels

When an incident photon (γ- or X-ray) interacts with an electron within the depletion region, mainly via photoelectric effect or Compton scattering, this primary electron then ionizes nearby atoms releasing more electron-hole pairs. Consequently, these charge carriers drift in opposite directions towards the corresponding electrodes because of the electric field and may be collected at the same time by several adjacent pixels, resulting in a "cluster".

Therefore, each registered cluster can be directly associated to the original photon interaction. This means that each cluster is equivalent to a "count" for conventional radiation detectors. In addition, the whole charge created by any incident photon can be revealed by summation of the fractional charges collected by all the pixels forming its associated cluster. The extent of charge sharing effect generally depends on the incident photon energy, pixel size, substrate layer, applied bias voltage, and the interaction depth within the sensitive volume [16].

A "cluster reconstruction" method (see figure 4) has been applied to correct for the above charge sharing effect. This method consists of determining the span of each registered cluster and defining the associated pixel with the highest ToT value as the possible location on the sensor surface of the original photon interaction. All the registered clusters can then be reduced to just the origin interaction pixels, improving the precision of the measurement. Furthermore, when using the ToT mode, the reading value of all the nearby pixels forming a given cluster can be summed to return the total energy deposited by the primary incident photon.

The method of cluster reconstruction also allows for a direct integration of the whole clusters registered along successive frames taken during the same measurement. Therefore, the number of registered clusters divided by the detection "live-time" (i.e., the preset shutter-time multiplied by the total recorded frames) directly provides the conventional "count rate" or "cps".

In principle, as illustrated in figure 4, both ToT and MPX modes are able to generate similar count rates under identical irradiation conditions. The only difference in MPX mode is that, as all the pixels associated to a given cluster provide the same reading value (one hit or 1), an arbitrary criterion regarding the possible location of the original photon interaction must be applied. This is why the cluster reconstruction step in the MPX mode is represented in figure 4 with a hatched arrow.

2016 JINST 11 P08012

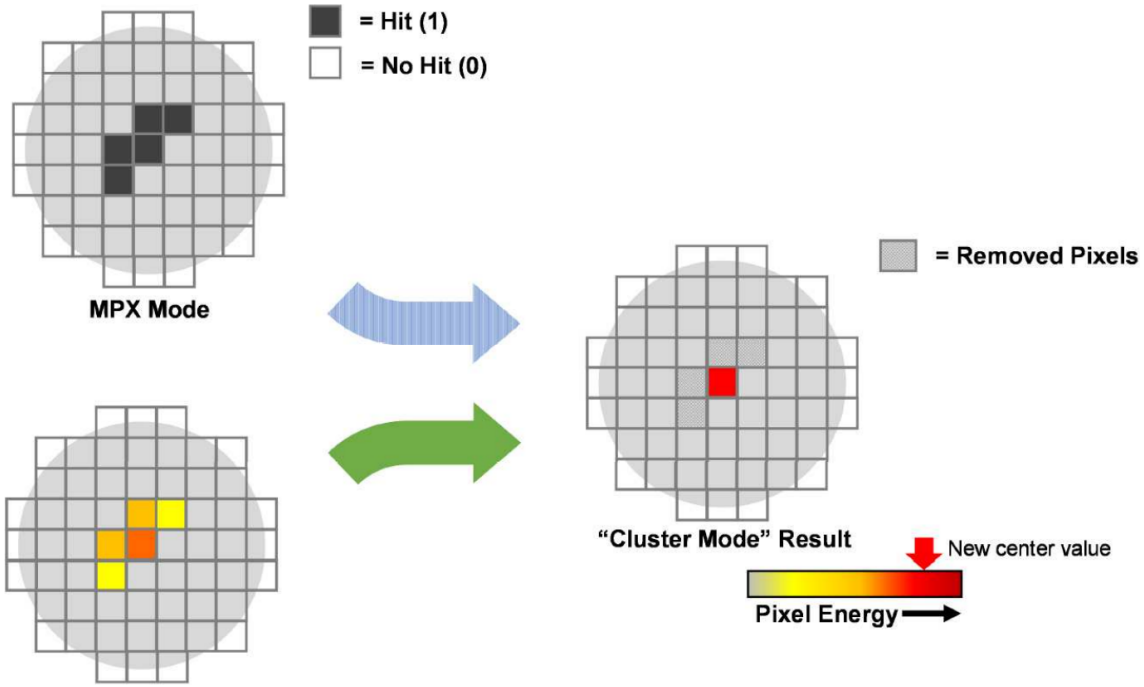

Figure 4. Example of application of the "cluster reconstruction" method.

2.1.3 Pixel output signal

The pixel output signal is approximated to a triangular pulse, with ~100 ns rise time and a fall time that can reach several tens of microseconds for the photon energy of interest, ranging between 10 keV and 1.5 MeV. Due to this triangular shape, the time duration (i.e., the number of clock cycles divided by the clock frequency in ToT mode) of any pixel output signal above the pre-set threshold level remains proportional to its voltage amplitude, which in turn is directly related to the portion of the total energy deposited by the incident photon that has been transferred to the considered pixel.

To have an idea how the ToT value varies with the associated energy deposited by the incident photon, figure 5 illustrates the example of single-pixel clusters. The green curve in this figure puts into evidence that the resulting ToT-energy calibration curve can be generally described by the following non-linear function depending on four parameters (a, b, c and d):

$$E_\gamma = f\,(\mathrm{ToT}) = a\mathrm{ToT} + b - \frac{c}{\mathrm{ToT} - d}\,. \tag{2.1}$$

This function has been experimentally confirmed by Jakubek et al. [17] showing a linear behaviour down to a given critical energy (usually near 10 keV) because of the threshold level that must be applied to avoid unwanted leakage current contribution (see section 2.1.6). Below this critical energy, the calibration curve deviates from linearity.

2.1.4 Pulse pile-up under intense photon fluxes

Under an excessive photon flux, the detector becomes saturated resulting in the pulse pile-up phenomenon. As illustrated in figure 6, when successive pulses are very close in time the system will wrongly record them as a single count with combined amplitude.

2016 JINST 11 P08012

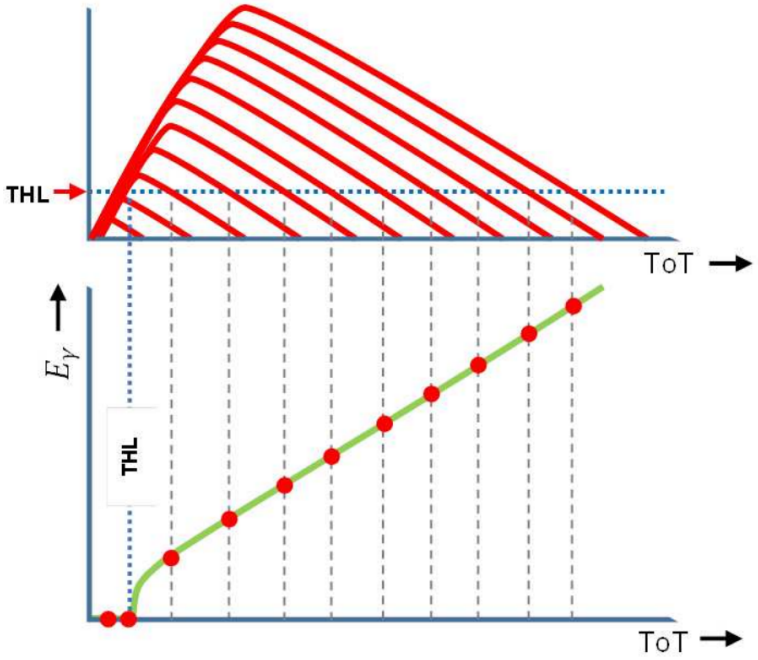

Figure 5. ToT value vs. full deposited gamma energy for single-pixel clusters.

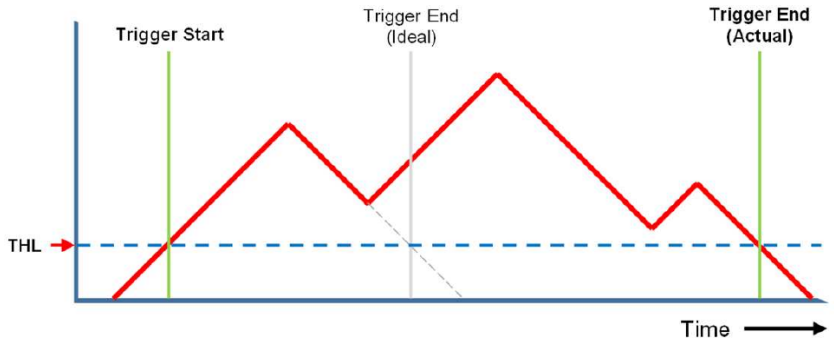

Figure 6. Illustration of the pulse pile-up effect.

2.1.5 Pulse summation due to extended shutter-times

When selecting an excessive shutter-time, even in case of a low incident photon flux, successive signals can be collected and accumulated before it expires (see figure 7). The resulting reading value under ToT mode is the sum of all of the individual signals that are detected on the particular pixel within this excessive shutter-time.

For this purpose, the shutter-time must be conveniently chosen to avoid this effect. If successive signals are recorded on the same pixel under ToT mode, the corresponding reading would lead to a meaningless numerical value. This effect can be minimized by decreasing the shutter-time to a limit of not setting it shorter than the time it takes for the pulse to be fully collected by the pixel. In addition, a very short shutter-time has a great risk of not providing enough statistics, especially at low photon fluxes. The iPIX response dependence with regards to the pre-set shutter-time is further explored in section 3.1.

2016 JINST 11 P08012

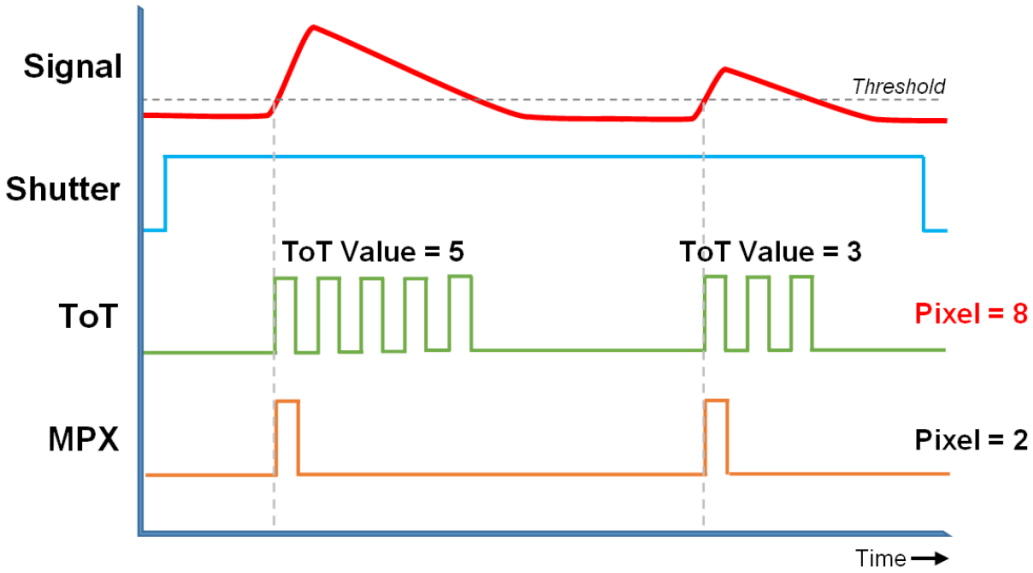

Figure 7. Summation of succeeding pulses due to excessive shutter-time.

2.1.6 Threshold equalization

Threshold equalization is used to compensate the pixel-to-pixel threshold variations of the Timepix readout chip due to local transistor mismatches. This procedure is normally applied using the inherent electronic noise as a trigger (i.e., the measurement is carried out in a radiation-free environment). In that case, the system tries to automatically fine-tune the 4-bit DAC offset for every pixel to be as close as possible to an optimum threshold level common to all pixels so that unwanted leakage current contribution is conveniently discarded but not the input pulses of interest.

A new equalization method was specifically developed for iPIX to well fix the leaking current issue. This method considers the real sensor response, instead of the inherent electronic noise, under a homogeneous X- or γ-ray flux in the energy range between 50–100 keV.

2.2 Coded-aperture mask

Three coded-aperture masks, providing two different mask ranks (see figure 8) and three different thicknesses, are currently available for the iPIX platform. They are identified according to their rank and thickness: R7e4, R7e8 and R13e2. The label "e" is an abbreviation of the word *épaisseur* (a French translation of "thickness"). Their planar area is four times that of the CdTe detector and their patterns were designed according to the well-known uniformly redundant arrays [18].

The benefit of a high mask rank is a more precise angular resolution with counterpart a decrease of the detection efficiency due to its less open area. Whereas increasing the mask thickness provides more photon filtering thus enhancing the signal-to-noise ratio but, in turn, it reduces the iPIX off-axis response (see section 3.7 for more details). The two masks of rank 7 can be inverted by a 90° rotation to perform anti-mask measurements. The application of the mask R13e2 is only limited for low photon energies. More specifically, this mask is used to detect the presence of plutonium in nuclear wastes via the 59 keV γ-ray of ^{241}Am.

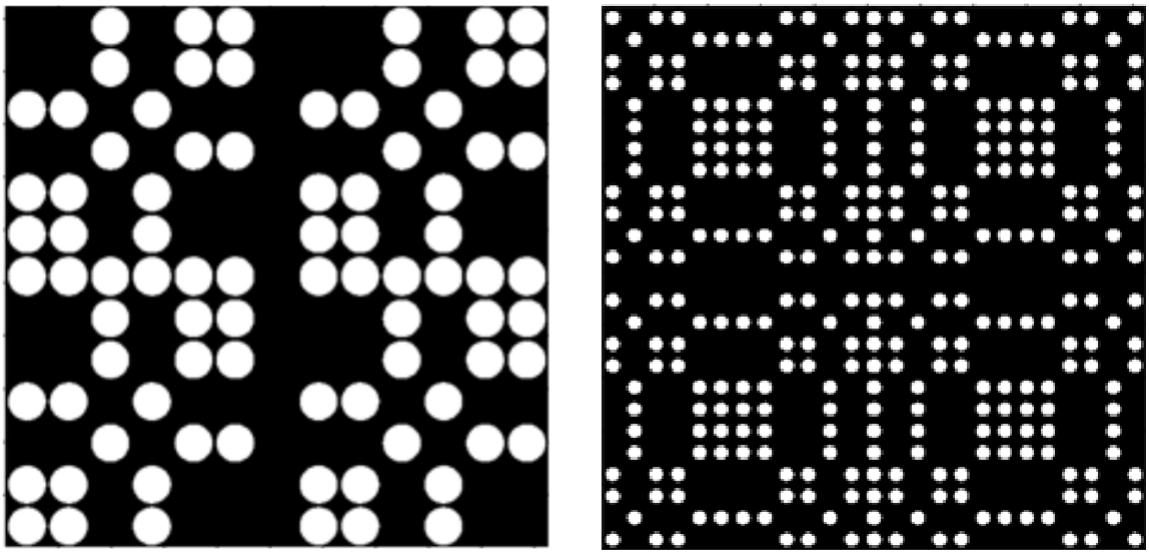

Figure 8. Pattern designs for the iPIX coded-aperture masks with rank 7 (left) and rank 13 (right).

By placing the coded-aperture mask in front of a photon beam, emitted from a given radioactive hotspot located within its field-of-view (FOV), a shadow of the "illuminated" portion of its pattern is cast onto the detector surface. It is thus necessary to apply a de-convolution process of the resulting data collected with the Timepix chip to accurately reconstruct the location of the radioactive hotspot on the scene under study. The interested reader is referred to [18] and [19] for more information about the mathematical rules behind the coded-aperture technique.

2.3 Irradiation set-up

The iPIX experimental characterisation has been carried out at by means of the wide-range irradiation equipment located at CANBERRA's Loches site as well as the KIT X-ray irradiation facility.

The CANBERRA irradiation equipment (figure 9) consists of:

1. A "big" irradiator with six interchangeable standard ^{137}Cs sources of nominal activities between 3 GBq and 30 TBq to provide a dose rate ranging from 20 μSv/h to 20 Sv/h at several source-to-detector distances.

2. A "small" irradiator with two interchangeable standard ^{137}Cs (~300 MBq) and ^{60}Co (~70 MBq) sources to provide a dose rate at the chosen measurement point ranging from 2 μSv/h to 100 μSv/h.

3. A "portable" irradiator based on a standard ^{241}Am source with ~1.85 GBq nominal activity to provide a dose rate ranging from 1 to 50 μSv/h.

The KIT X-ray irradiation facility (figure 10) is equipped with secondary standards and is able to provide the ISO standard narrow beams or N-Series [13]. All the X-ray beams used in this study, together with their theoretical energy distributions, are listed in table 1 and table 2. Increasing input

2016 JINST 11 P08012

Table 1. ISO X-ray narrow beams (15–60 kV) together with the measured ambient dose equivalent rates at varied input currents (details are given in the text).

ISO reference	Distance	Beam Inputs		Mean Energy	$\dot{H} * (10)$ (mSv/h)	Energy Spectrum (reproduced from ref. [13])
		Voltage	Current			
N-15	200 cm	15 kV	1 mA	13.3 keV	0.34 ± 0.02	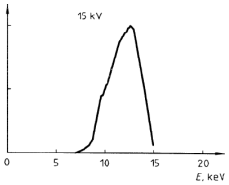
			5 mA		1.64 ± 0.08	
			10 mA		3.27 ± 0.16	
			15 mA		4.91 ± 0.25	
			20 mA		6.56 ± 0.33	
N-20	200 cm	20 kV	1 mA	16.9 keV	1.58 ± 0.08	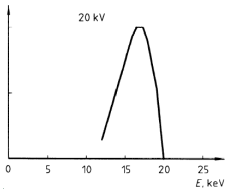
			5 mA		7.89 ±0.39	
			10 mA		15.72 ± 0.79	
			15 mA		23.6 ± 1.2	
			20 mA		31.5 ± 1.6	
N-30	200 cm	30 kV	1 mA	24.6 keV	1.83 ± 0.09	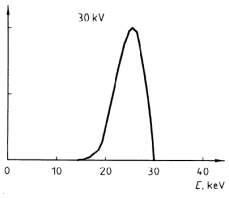
			5 mA		9.23 ± 0.46	
			10 mA		18.44 ± 0.92	
			15 mA		27.5 ± 1.4	
			20 mA		36.8 ± 1.8	
N-40	200 cm	40 kV	1 mA	33.0 keV	3.91 ± 0.19	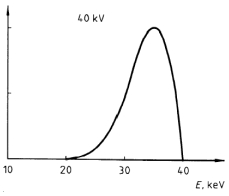
			5 mA		19.51 ± 0.98	
			10 mA		38.5 ± 1.9	
			15 mA		57.3 ± 2.9	
			20 mA		76.2 ± 3.8	
N-60	200 cm	60 kV	1 mA	47.6 keV	2.59 ± 0.13	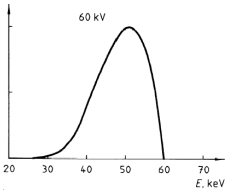
			5 mA		13.15 ± 0.66	
			10 mA		26.5 ± 1.3	
			13 mA		34.5 ± 1.7	

Table 2. ISO X-ray narrow beams (80–300 kV) together with the measured ambient dose equivalent rates at varied input currents (details are given in the text).

ISO Reference	Distance	Beam Inputs		Mean Energy	$\dot{H}*(10)$ (mSv/h)	Energy Spectrum (reproduced from ref. [13])
		Voltage	Current			
N-80	200 cm	80 kV	1 mA	65.3 keV	1.45 ± 0.07	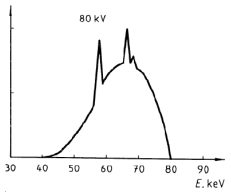
			5 mA		7.47 ± 0.37	
			10 mA		14.93 ± 0.75	
			13 mA		19.42 ± 0.97	
N-100	200 cm	100 kV	1 mA	83.8 keV	0.57 ± 0.03	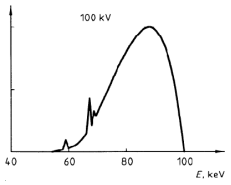
			5 mA		2.91 ± 0.16	
			10 mA		5.83 ± 0.29	
			13 mA		8.03 ± 0.40	
N-150	200 cm	150 kV	1 mA	118.4 keV	5.00 ± 0.25	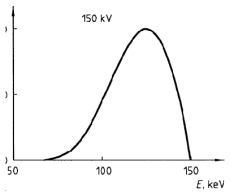
			5 mA		25.4 ± 1.3	
			10 mA		50.6 ± 2.5	
			13 mA		67.7 ± 3.4	
N-200	200 cm	200 kV	1 mA	164.5 keV	1.78 ± 0.09	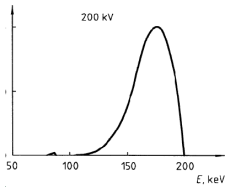
			5 mA		9.14 ± 0.46	
			10 mA		18.68 ± 0.93	
			13 mA		24.2 ± 1.2	
N-250	200 cm	250 kV	1 mA	207.3 keV	1.75 ± 0.09	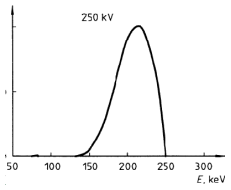
			5 mA		9.00 ± 0.46	
			10 mA		18.02 ± 0.93	
			13 mA		22.8 ± 1.2	
N-300	200 cm	300 kV	1 mA	247.5 keV	1.59 ± 0.08	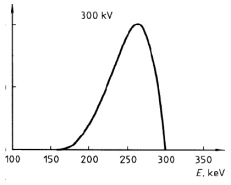
			5 mA		8.37 ± 0.42	
			10 mA		16.87 ± 0.84	
			13 mA		22.2 ± 1.1	

2016 JINST 11 P08012

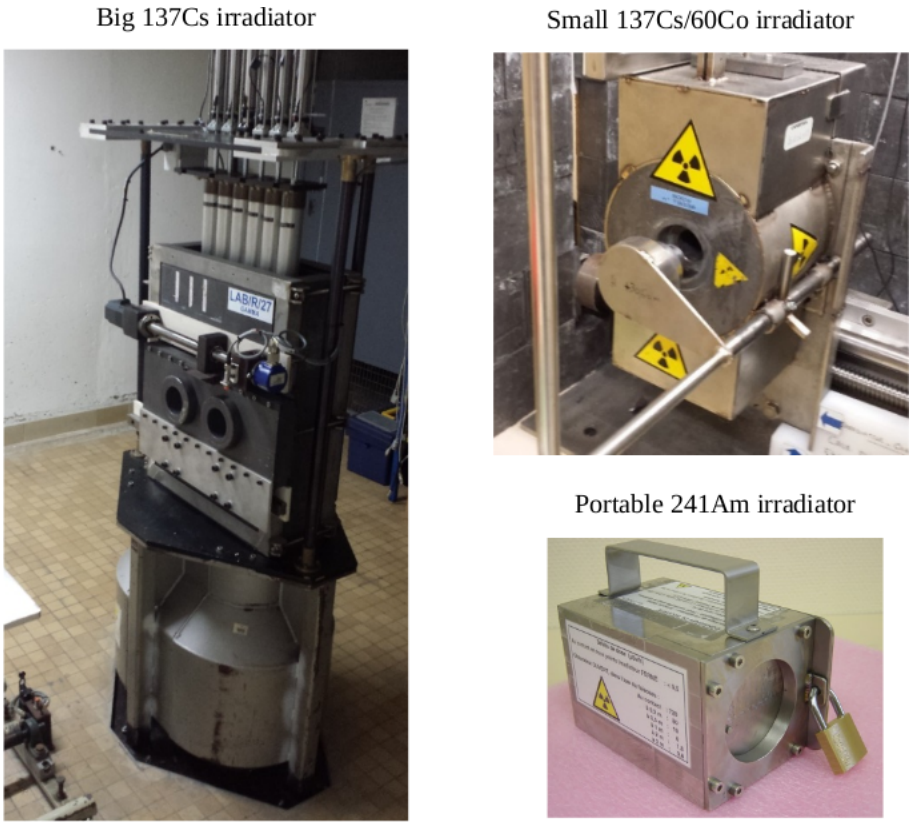

Figure 9. CANBERRA irradiation equipment.

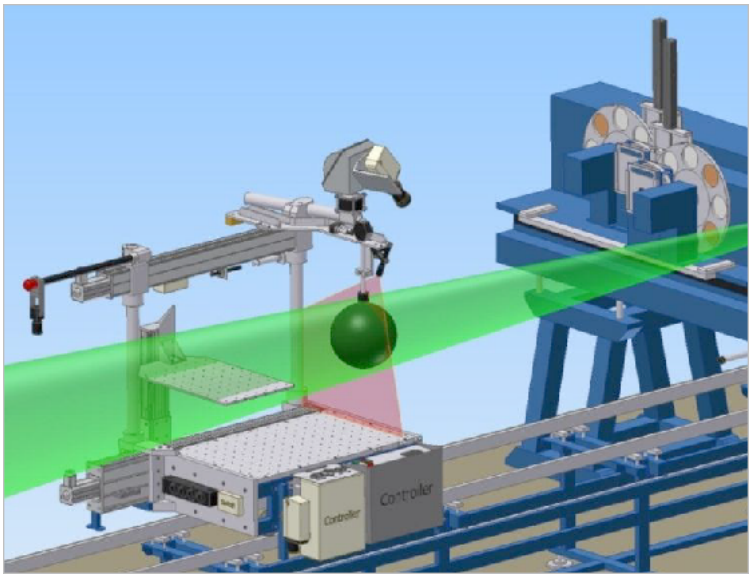

Figure 10. Drawing of the KIT X-ray irradiation facility with a reference ionization chamber located at the measurement point.

2016 JINST 11 P08012

electron currents were applied for each X-ray energy (i.e., at constant acceleration voltages in kV) in order to increase the associated flux at the considered measurement point.

For each irradiation run at the KIT X-ray irradiation facility, the following steps have been essentially used for the determination of the iPIX response to X-ray beams:

- Firstly, a basic quantity such as air Kerma rate or $\dot{K}_{\text{air}}$ expressed in mGy/h units was directly measured with a calibrated ionization chamber at the considered distance (~2 meters).
- Then, the appropriate operational quantity, in terms of the ambient dose equivalent rate or $\dot{H}*(10)$ expressed in mSv/h units, was derived by the application of the associated conversion coefficient derived from ICRP-74 [20]. The corresponding values for every X-ray beam at varied input currents are summarized in tables 1 and 2.
- Lastly, the iPIX device under test was placed at the same measurement distance to evaluate its response.

Almost the same steps were followed at CANBERRA irradiation facilities with the only difference of using the calibrated ionization chamber earlier before at five reference distances for the considered standard source to derive the associated fitting parameters (a and b) of the following empirical relationship:

$$\dot{K}_{\text{air}} = a x^{-b} \tag{2.2}$$

where x is the source-to-detector distance in cm.

3 Results and discussion

3.1 Data quality

In this section, a qualitative study of the measurement data collected at the KIT X-ray facility is performed. In this case, the iPIX count rates measured at each X-ray beam have been normalized to the corresponding dose rate (see tables 1 and 2) in order to facilitate comparison between the different shutter-times used. Indeed, when increasing the X-ray beam currents the whole area of the measured spectra must be linearly proportional to the associated dose rates.

As expected, the masks R7e8 and R7e4 provide quite similar results whereas the ones obtained with R13e2 when the incident photon energy is above 200 keV were quite unsatisfactory (i.e., the radioactive hotspot is not anymore localized) due to its small thickness. The iPIX measurement data collected with the mask R7e8 are plotted in figures 11–21 to show the typical evolution of the cluster ToT distributions with respect to the incident X-ray beam energy and current as well as to the Timepix shutter-time.

According to these figures, when the shutter-time is appropriately chosen to avoid signal distortions eventually due to pulse pile-up and/or summation effects, as explained in sections 2.1.4 and 2.1.5, the associated count rates per unit of mSv/h must not change when only the X-ray beam current is varied. This is the case when 10^{-4} sec shutter-time is chosen for all the considered ISO X-ray narrow beams and at practically the whole range of applied currents.

Conversely, caution should be taken when choosing a shutter-time of 10^{-5} sec since it cannot be applied for photon energies above 150 keV. In fact, above this energy, the effect of incomplete

2016 JINST 11 P08012

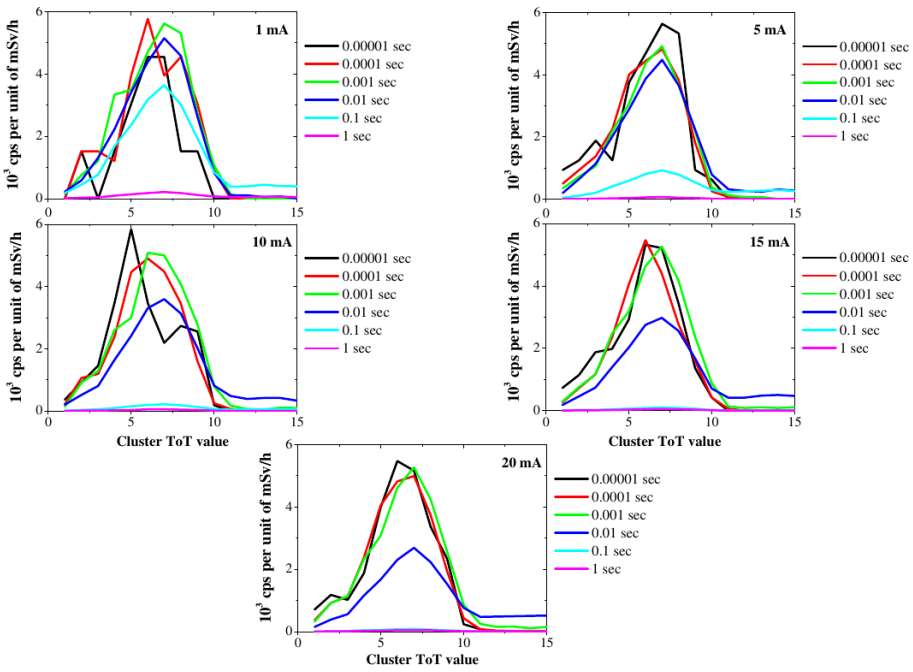

Figure 11. Cluster ToT distributions measured with the mask R7e8 under different shutter-times for the N-15 (E_{mean} = 13.3 keV) X-ray narrow beams of varied currents. Owing to the photoelectric process there is a single full-energy peak.

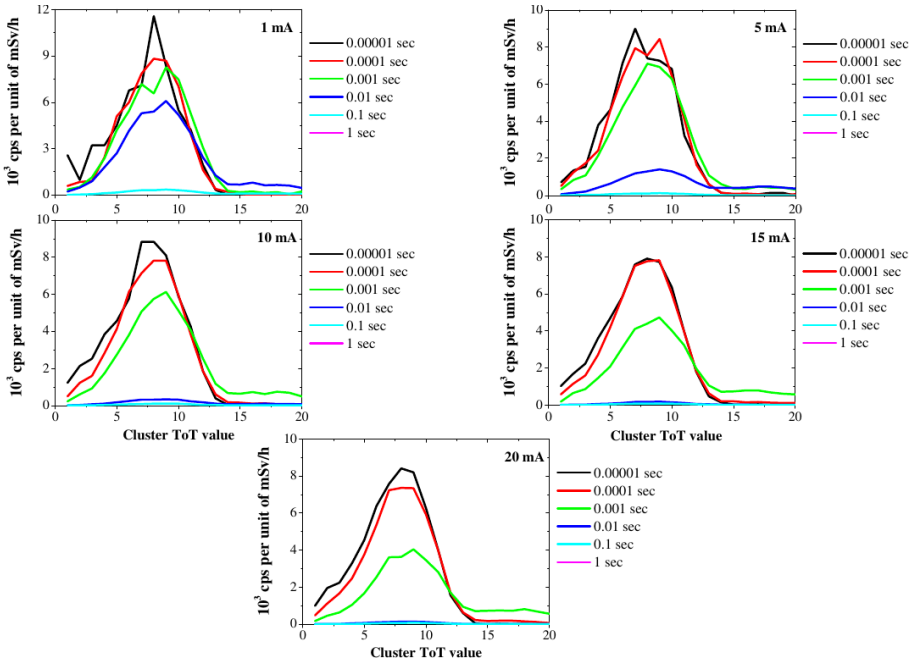

Figure 12. Cluster ToT distributions measured with the mask R7e8 under different shutter-times for the N-20 (E_{mean} = 16.9 keV) X-ray narrow beams of varied currents. Owing to the photoelectric process there is a single full-energy peak.

2016 JINST 11 P08012

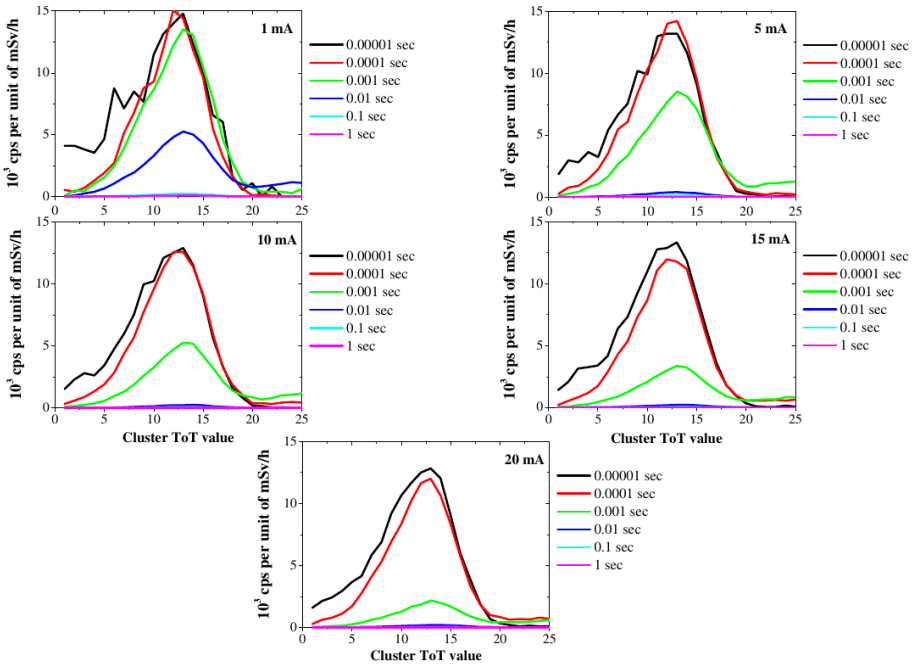

Figure 13. Cluster ToT distributions measured with the mask R7e8 under different shutter-times for the N-30 (E_{mean} = 24.6 keV) X-ray narrow beams of varied currents. Owing to the photoelectric process there is a single full-energy peak.

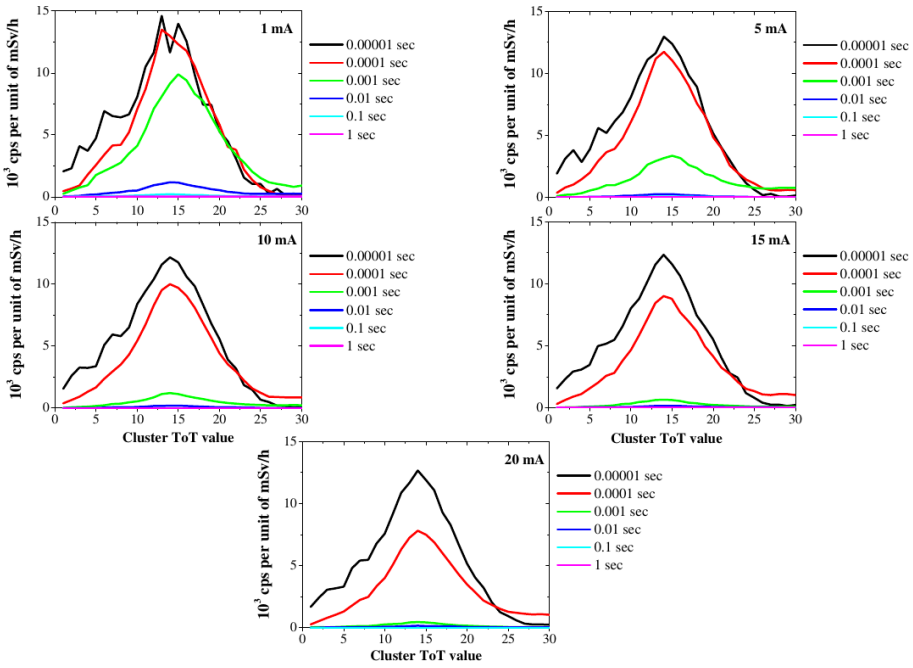

Figure 14. Cluster ToT distributions measured with the mask R7e8 under different shutter-times for the N-40 (E_{mean} = 33.0 keV) X-ray narrow beams of varied currents. Owing to the photoelectric process there is a single full-energy peak.

2016 JINST 11 P08012

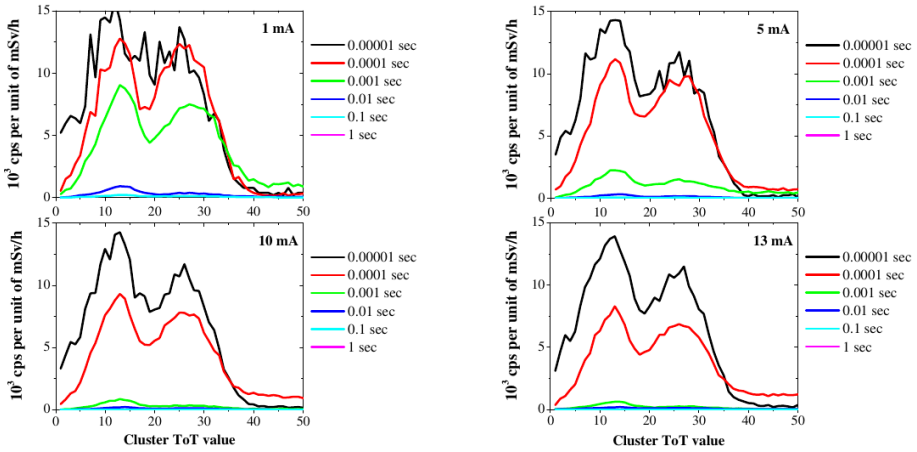

Figure 15. Cluster ToT distributions measured with the mask R7e8 under different shutter-times for the N-60 (E_{mean} = 47.6 keV) X-ray narrow beams of varied currents. Besides the full-energy peak, an additional one appears on the left at around 13 ToT (i.e., ∼1.4 μsec).

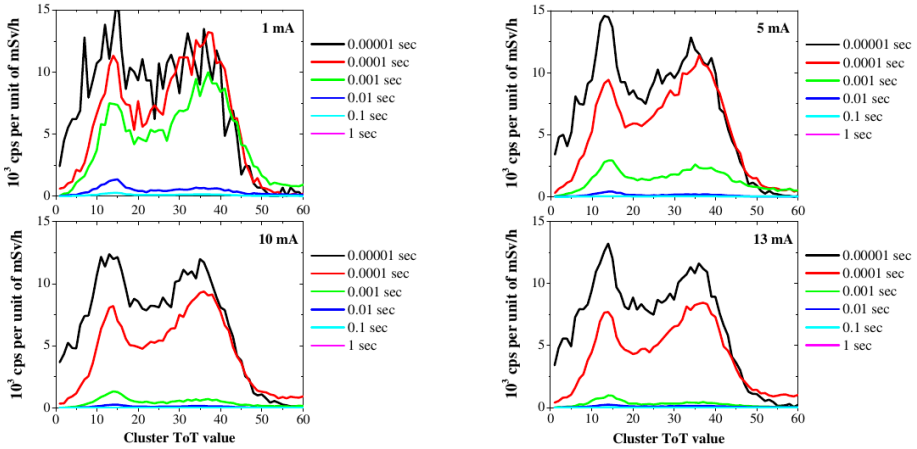

Figure 16. Cluster ToT distributions measured with the mask R7e8 under different shutter-times for the N-80 (E_{mean} = 65.3 keV) X-ray narrow beams of varied currents. Unlike the full-energy peak, the additional one does not move to the right with increasing the incident photon energy.

charge collection of the pixel output signals becomes apparent. Shutter-times higher than 10^{-4} sec can only be applied for a limited range of X-ray beams and at very low currents with the exception of 1 sec that completely failed in providing physically meaningful results.

Furthermore, a clear distinction has always to be made between radioactive hotspot localization (possible even under pulse pile-up and/or summation effects) and dose rate evaluation that can be done only when dose rate linearity is fully guaranteed.

It must be noticed that interactions of low energy photons with the CdTe substrate occur primarily via the photoelectric process giving rise to a single full-energy peak, which as expected shifts to higher ToT values with increasing the beam acceleration voltage. When the incident photon energy is above 40 keV, an additional peak appears on the left at around 13 ToT (i.e., ∼1.4 μsec) as shown in figure 15. In the beginning, we believed that it is a consequence of the possible

2016 JINST 11 P08012

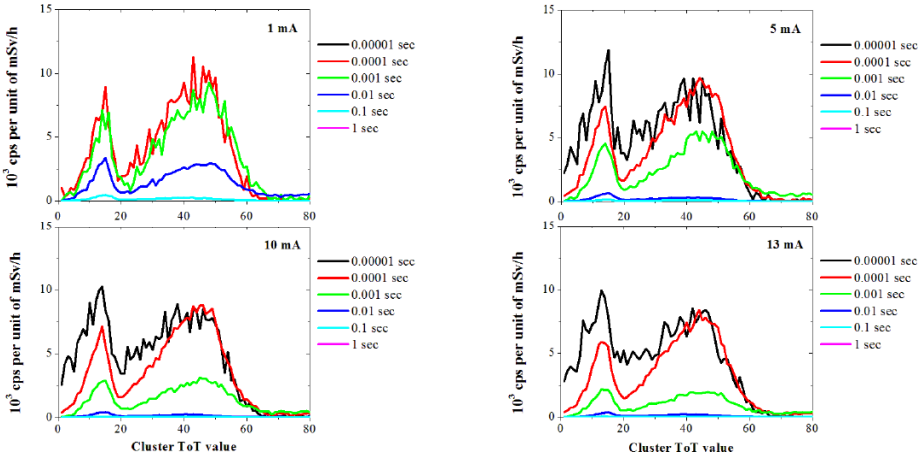

Figure 17. Cluster ToT distributions measured with the mask R7e8 under different shutter-times for the N-100 (E_{mean} = 83.8 keV) X-ray narrow beams of varied currents. Data obtained with a 10^{-5} sec shutter-time and at low (1 mA) beam input current were statistically insignificant and are not reproduced here. Unlike the full-energy peak, the additional one does not move to the right with increasing the incident photon energy.

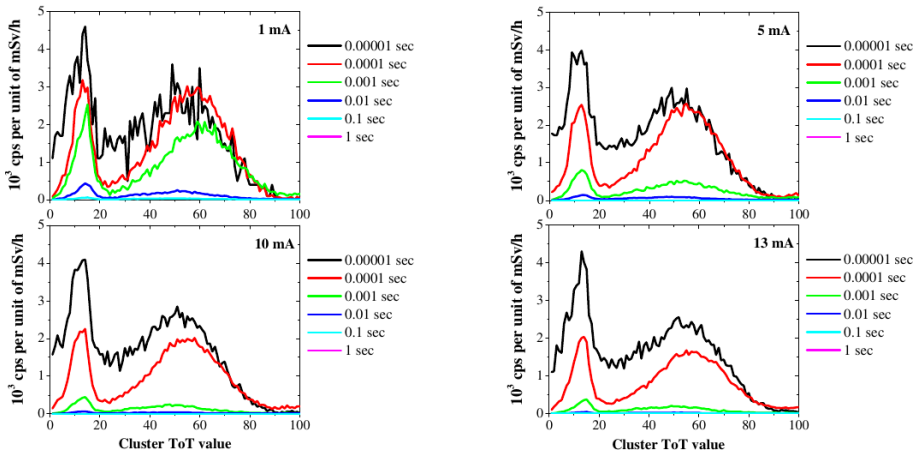

Figure 18. Cluster ToT distributions measured with the mask R7e8 under different shutter-times for the N-150 (E_{mean} = 118.4 keV) X-ray narrow beams of varied currents. Unlike the full-energy peak, the additional one does not move to the right with increasing the incident photon energy.

escape from the detector sensitive volume of characteristic fluorescence X-rays (23–31 keV) locally emitted by Cd or Te atoms after photoelectric interactions. Nevertheless, this peak remains fixed and contrary to the full-energy peak it does not move to the right with increasing the incident photon energy. For this reason, we think that it could be a direct detection of extra characteristic fluorescence X-rays emitted by other elements outside the CdTe substrate. The lack of knowledge about the actual composition of all surrounding materials does not allow us to make any kind of prediction regarding this additional peak.

2016 JINST 11 P08012

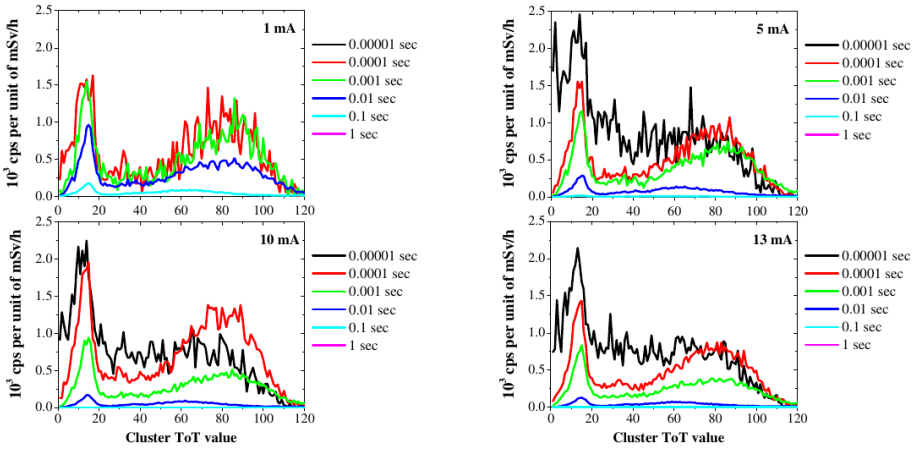

Figure 19. Cluster ToT distributions measured with the mask R7e8 under different shutter-times for the N-200 (E_{mean} = 164.5 keV) X-ray narrow beams of varied currents. Data obtained with a 10^{-5} sec shutter-time and at low (1 mA) beam input current were statistically insignificant and are not reproduced here. Unlike the full-energy peak, the additional one does not move to the right with increasing the incident photon energy.

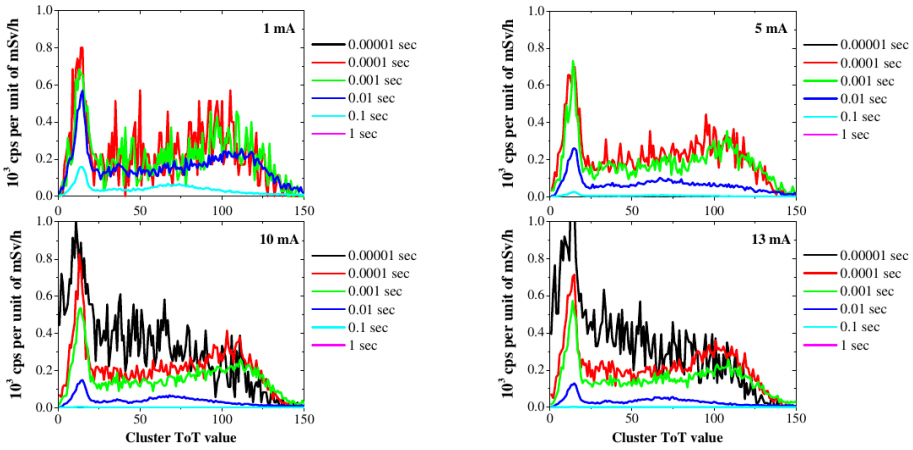

Figure 20. Cluster ToT distributions measured with the mask R7e8 under different shutter-times for the N-250 (E_{mean} = 207.3 keV) X-ray narrow beams of varied currents. Data obtained with a 10^{-5} sec shutter-time and at low (1 mA) beam input current were statistically insignificant and are not reproduced here. The measurement files for 10^{-5} sec shutter-time and 5 mA beam input current were corrupted. The full-energy peak is no longer visible whereas the additional one is still appearing.

3.2 ToT-energy calibration

Only clearly differentiated and sharp full-energy peaks were considered for the ToT-energy calibration. This was the case for the incident photon mean energies ranging from 10 to 90 keV and 10^{-4} sec shutter-time (see figures 11–17). Each one of these peaks was fitted with a Gaussian function to derive the associated ToT value of its geometric centre. The results obtained are plotted in figure 22, where all the ToT values were divided by the default clock frequency to express them in time units. A satisfying linearity is observed between incident photon energies and their respective ToT values.

Figure 23 shows the measured ^{137}Cs spectrum after applying the ToT-energy calibration rela-

2016 JINST 11 P08012

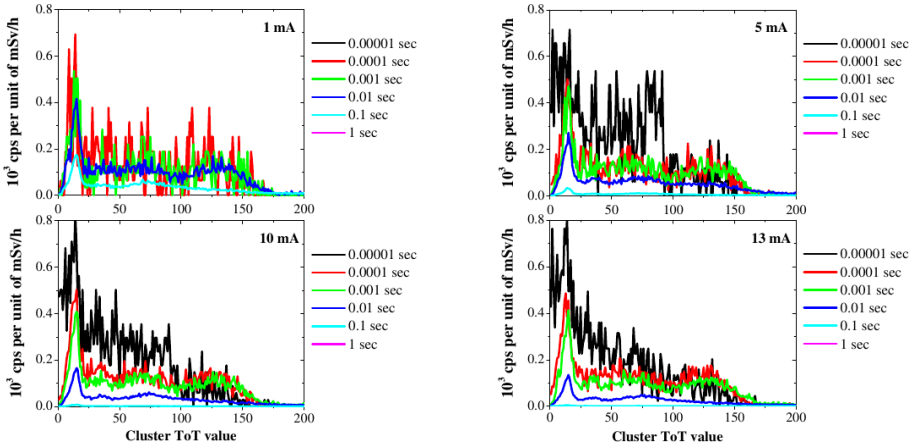

Figure 21. Cluster ToT distributions measured with the mask R7e8 under different shutter-times for the N-300 (E_{mean} = 247.5 keV) X-ray narrow beams of varied currents. Data obtained with a 10^{-5} sec shutter-time and at low (1 mA) beam input current were statistically insignificant and are not reproduced here. The full-energy peak is no longer visible whereas the additional one is still appearing.

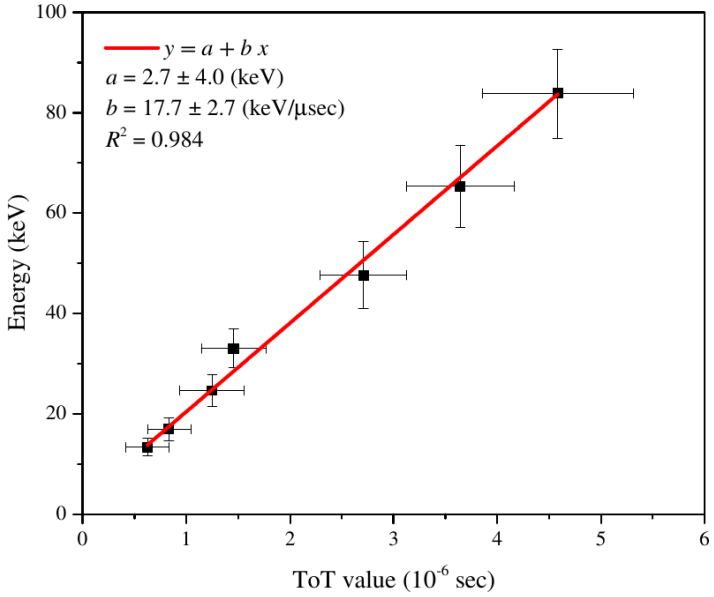

Figure 22. ToT-photon energy calibration curve for the iPIX gamma camera.

tionship derived in figure 22. The chosen experimental conditions were a dose rate of 1 Sv/h at the measurement point and a total of 2000 frames (i.e., 1000 frames using the "mask" position and 1000 frames using the "anti-mask" position) with a shutter-time of 10^{-4} sec.

This figure makes easily distinguishable two full-energy peaks associated to 32 keV γ-ray of ^{137}Cs and to the characteristic fluorescence photons (58–85 keV) emitted from the tungsten (W) atoms in the coded-aperture mask and/or from the irradiator Pb-based collimator. The current energy resolution of the CdTe detector does not allow resolving W and Pb characteristic lines.

Despite the small thickness of the CdTe substrate, the corresponding 662 keV peak of ^{137}Cs as well as its Compton edge (~478 keV) are also visible on logarithmic scale (figure 23). This ultimately ratifies the validity of the ToT-energy linearity also at high energies. The energy resolution for the 662 keV peak was found to be approximately 9%.

2016 JINST 11 P08012

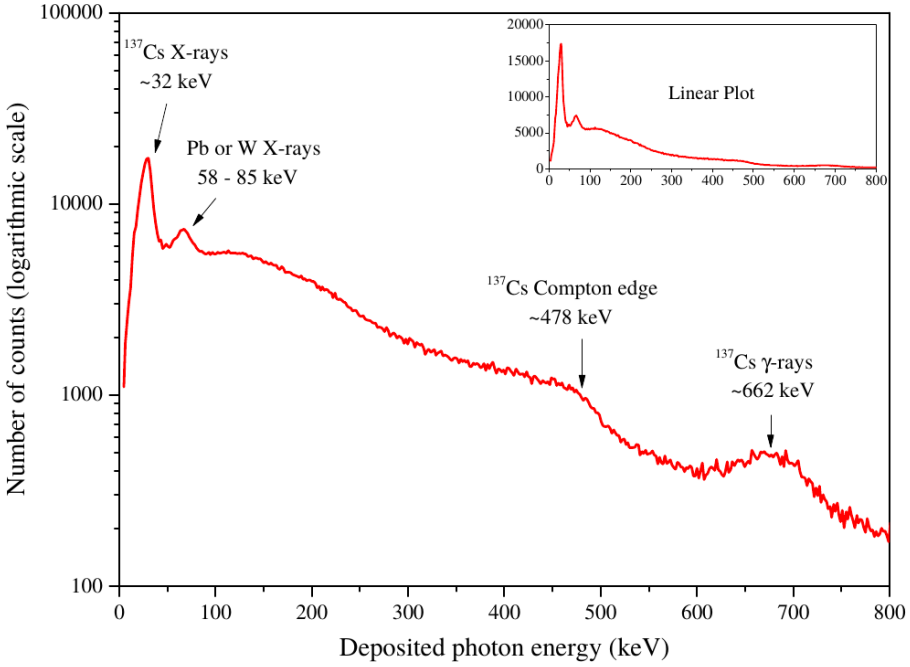

Figure 23. Measured ^{137}Cs spectrum with iPIX.

Similar ^{137}Cs spectra were obtained for other dose rates but considering highly significant statistics as well as appropriate shutter-times to avoid signal distortions due to pulse pile-up and/or summation effects (as explained in sections 2.1.4 and 2.1.5).

Taking into account the above ToT-energy calibration relationship, the expected ToT for the 1500 keV energy is ~85 μsec so that, as a general rule, the iPIX shutter-time should never decrease below 10^{-4} μsec to be sure that all pixel output signals generated in the photon energy range of interest (10 keV–1.5 MeV) will be fully recorded.

3.3 Dose rate linearity

The variation of the iPIX count rates with respect to the reference dose rates was studied at the CANBERRA big irradiator considering the two masks R7e4 (see figure 24) and R7e8. Again, these masks provide quite similar results. In fact, depending on the chosen shutter-time, almost all the dose rate response curves are linear along a given range until reaching a maximum, after which the radioactive hotspot is no longer localized. These curves finally drop off towards a full saturation of the Timepix detector when a single cluster containing all of its pixels is registered. It can be also seen in figure 24 that the iPIX dose rate response may be considered as quite linear over a wide range reaching nearly 8 decades (10^{-6}–10^{1} Sv/h) if the Timepix shutter-time is correctly chosen to avoid signal distortions due to pulse pile-up and/or summation effects.

3.4 Dose calibration factor vs. incident photon energy

The iPIX dose calibration factor is energy dependent and is defined as the number of the registered net counts per second (cps) divided by the photon ambient dose equivalent rate (in mSv/h units) at the measurement point. The corresponding values obtained for all the CANBERRA radioactive

2016 JINST 11 P08012

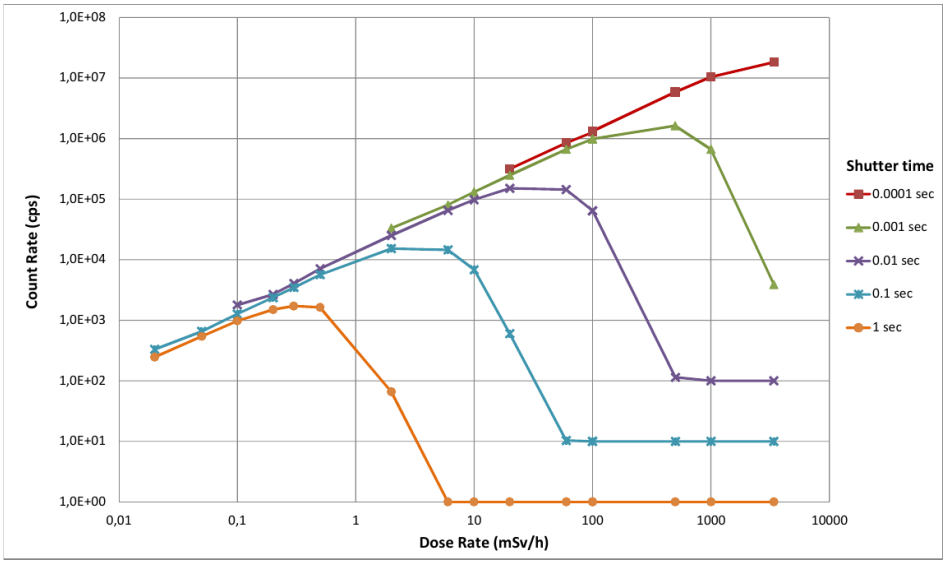

Figure 24. Dose response curves for the ^{137}Cs radioactive source measured directly with iPIX using the mask R7e4. A similar behaviour was also observed with the mask R7e8.

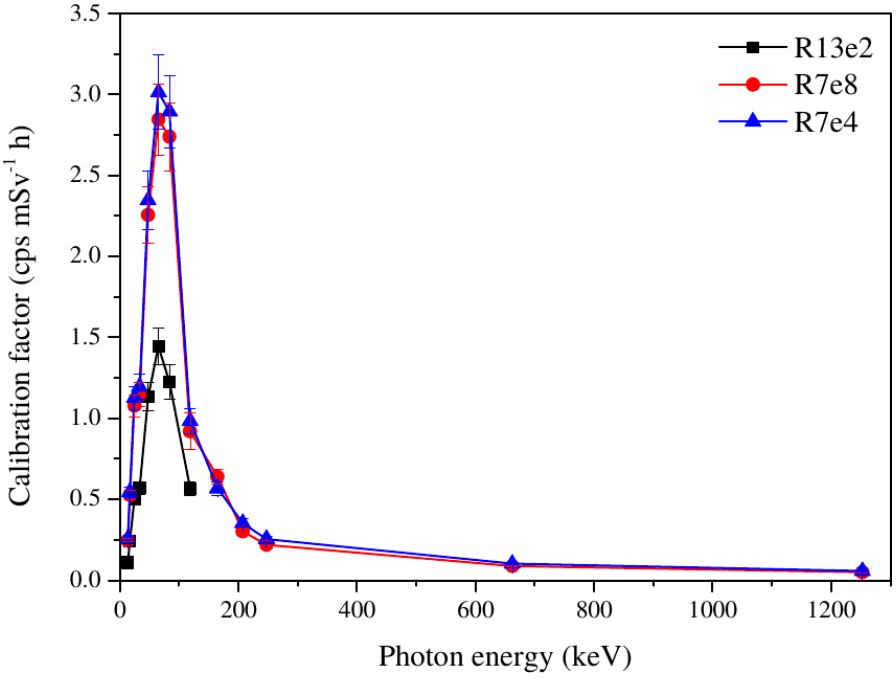

Figure 25. Dose calibration factor of the iPIX as a function of the incident photon energy.

sources as well as for the KIT X-ray narrow beams are displayed on figure 25. This figure shows that the two masks R7e4 and R7e8 provide quite similar response whereas that of R13e2 is almost two times lower as a result of its high rank as stated in section 2.2. On the other hand, the iPIX response behaviour with respect to the incident photon energy is fully consistent with figure 2. Indeed, the dose calibration factor for an ^{241}Am radioactive source is ~30 and ~50 times higher than for ^{137}Cs and ^{60}Co, respectively.

2016 JINST 11 P08012

3.5 Cluster sizes vs. incident photon energy

In this section, we examine the dependence of the cluster size with respect to incident photon energy. In each case, the shutter-time was appropriately chosen to avoid signal distortions on the Timepix detector due to pulse pile-up and/or summation effects. Once again, as all the coded-aperture masks provide quite similar results, only those obtained with the mask R7e8 are shown in figures 26 and 27.

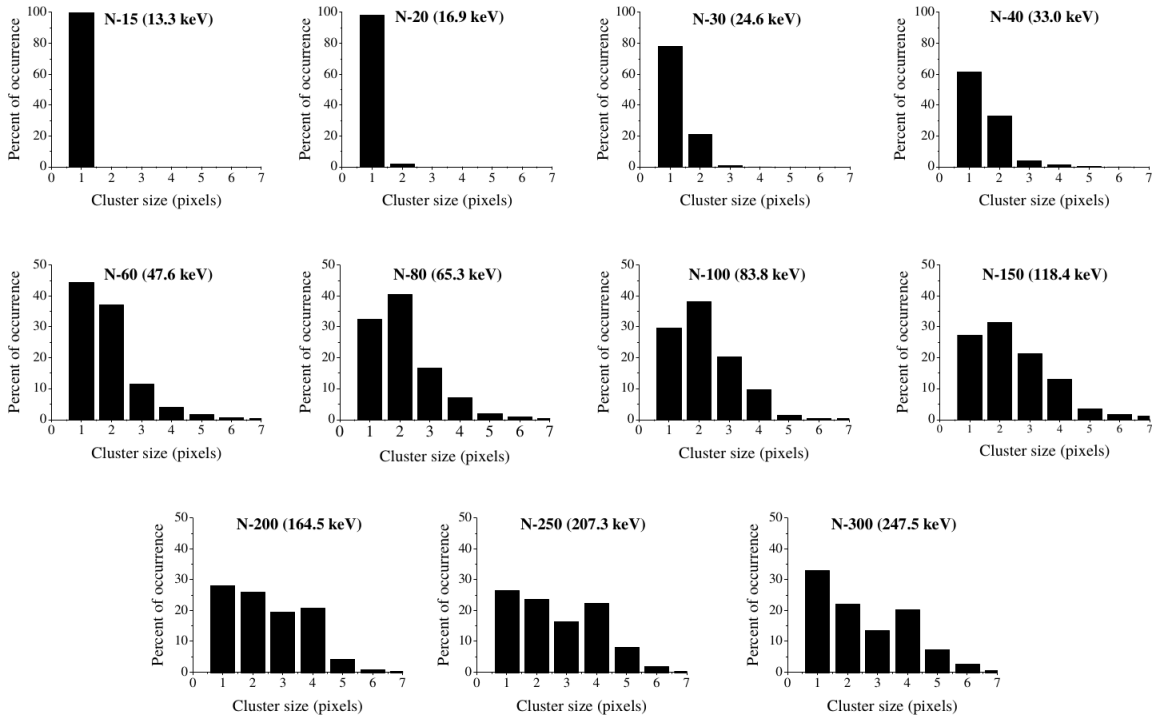

Figure 26. Cluster size distributions measured with the mask R7e8 for the X-ray narrow beams.

According to figure 26 a discrimination criterion, especially between low (e.g. ^{241}Am) and high photon energies (e.g. ^{137}Cs and ^{60}Co), can be applied but only for a qualitative analysis to estimate an energy range of the observed hotspot(s). Conversely, the same criterion is not practical to quantify the individual contribution of a given radionuclide to the overall dose rate as the cluster size distributions generated by different photon energies are significantly overlapping. In other words, there is not a clearly distinguishable signature in terms of cluster size distribution allowing both identification and quantification of radionuclides.

Another aspect to remark is that an upper size threshold of 20 pixels can be applied to discard unwanted cluster events such as the ones that may be generated by cosmic rays.

3.6 Sensitivity and influence of background radiation

The iPIX sensitivity has been studied with the low-activity point sources listed on table 3 but placing the CANBERRA small irradiator (figure 9) behind it in order to simulate, if needed, different background contributions. All the results obtained directly using the iPIX automatic

2016 JINST 11 P08012

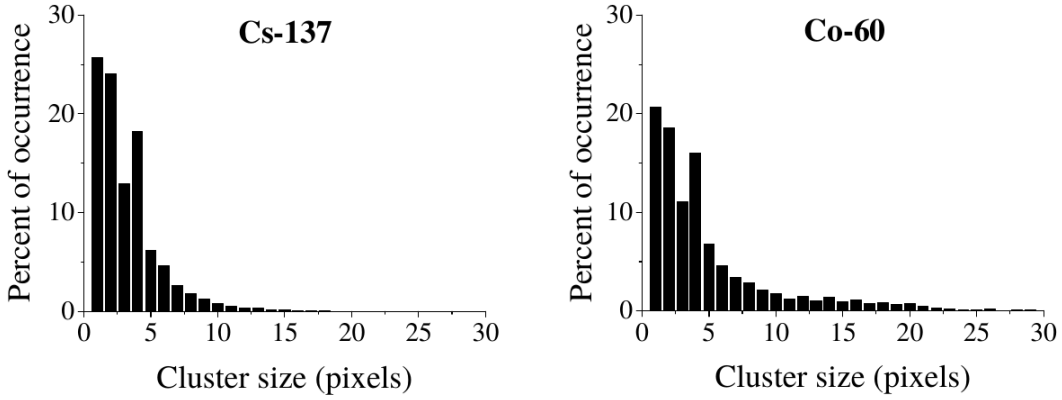

Figure 27. Cluster size distributions measured with the mask R7e8 for ^{137}Cs and ^{60}Co.

mode[1] and with the small irradiator entirely shielded are summarized in figures 28 and 30. Here, the natural background radiation dose rate at the iPIX location was previously monitored and it was within 0.1–0.2 μSv/h.

Table 3. Low-activity point sources used for sensitivity measurements.

Radionuclide	**Current activity**	**Distance**	**H∗(10)**
^{60}Co	226 kBq	22.3 cm	2 μSv/h
^{241}Am	412 kBq	48.0 cm	10 nSv/h
^{137}Cs	368 kBq	61.5 cm	100 nSv/h

Table 4. Minimum localization time (considering data collection only).

	^{241}Am (10 nSv/h)	^{137}Cs (100 nSv/h)	^{60}Co (2.0 μSv/h)
R13e2	50 sec	—	—
R7e4	4 sec	190 sec	70 sec
R7e8	—	120 sec	60 sec

It can be observed in these figures that iPIX, once positioned, was fully able to localize by itself — without any further actions from the user — all the low-activity sources listed in table 3. Two criteria must be usually satisfied to decide if a radioactive source is adequately localized: 1) apparition of a hotspot in a clean picture without any kind of interferences or misleading artifacts, and 2) the corresponding peak is quite differentiated in a 3D profile plot, which shows the registered counts associated to each Timepix pixel after the de-convolution process (see section 2.2). Another aspect to highlight is that the parallax correction is no longer possible at source-to-detector distances less than 50 cm (see the mismatch between the actual location of the considered radioactive sources and that of the associated colored hotspots as determined by iPIX in figures 28 and 29).

[1]Under which iPIX is able to autonomously select, among other parameters, the appropriate shutter-time and the minimum number of frames needed for every measurement environment.

2016 JINST 11 P08012

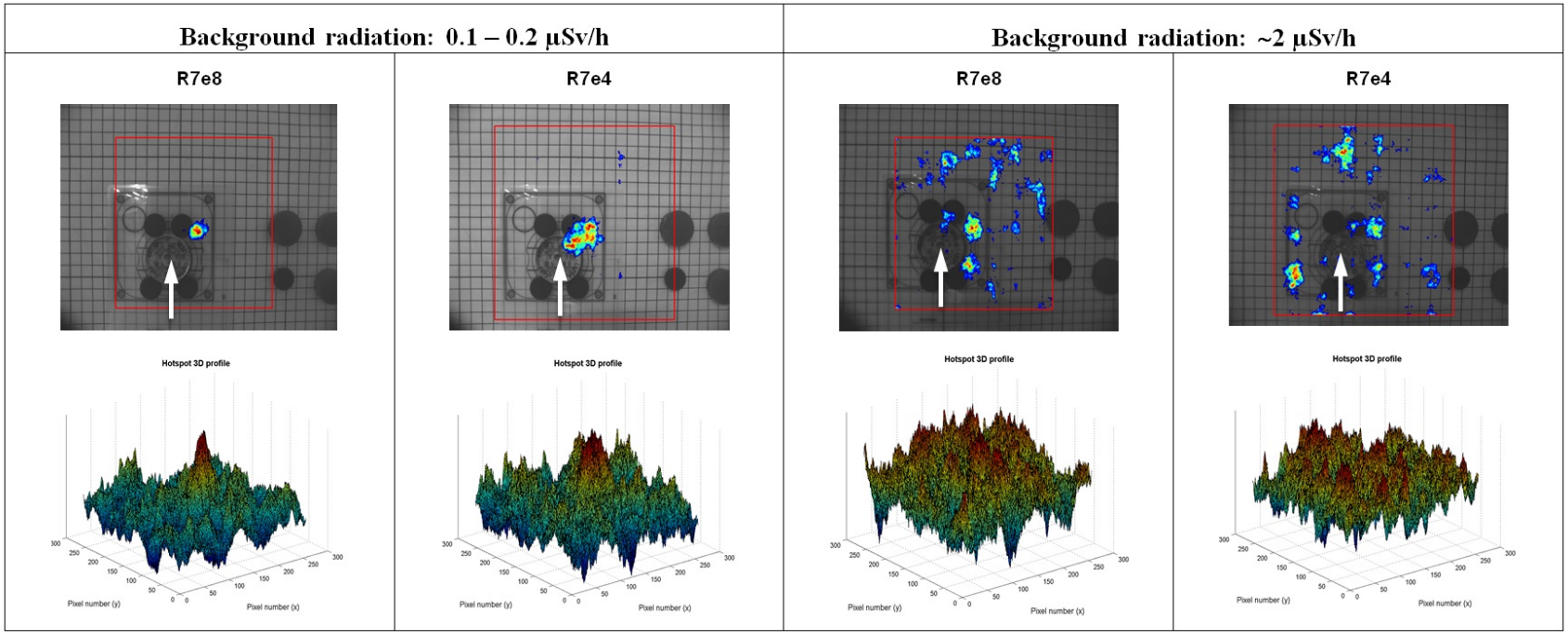

Figure 28. Measurement results of iPIX obtained with a 226 kBq ^{60}Co point source located at a distance of 22.3 cm with varied background radiation. The location of the considered radioactive sources are indicated by white arrows.

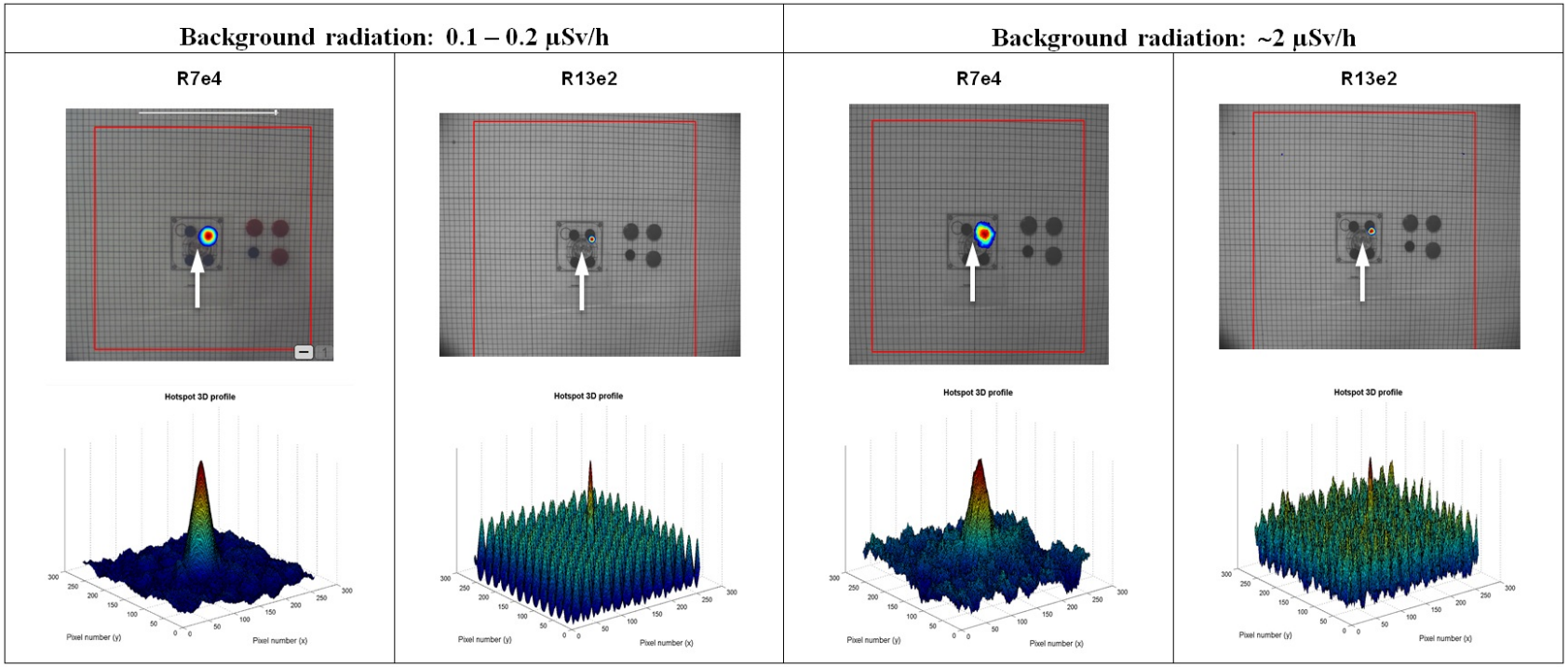

Figure 29. Measurement results of iPIX obtained with a 412 kBq ^{241}Am point source located at a distance of 48 cm with varied background radiation. The location of the considered radioactive sources are indicated by white arrows.

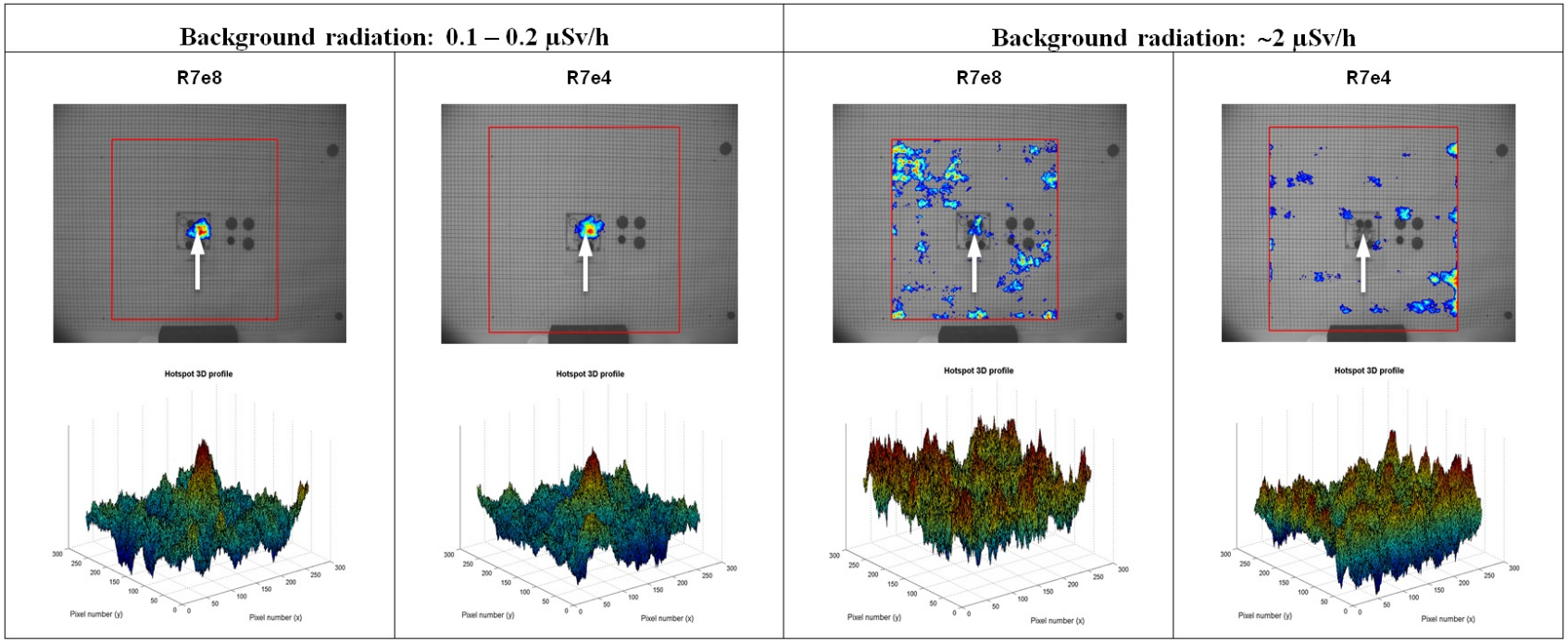

Figure 30. Measurement results of iPIX obtained with a 368 kBq ^{137}Cs point source located at a distance of 64.5 cm with varied background radiation. The location of the considered radioactive sources are indicated by white arrows.

The minimum times needed, considering data collection only, to localize the above low-activity point sources are summarized in table 4. In all cases, the mask R7e8 mask always gives the fastest localization time. Moreover, iPIX was able to localize the 412 kBq ^{241}Am point source, providing a dose rate at the measurement point of only 2 nSv/h, with a minimum of 70 frames of 1 sec shutter-time. Additional measurements were also carried out as shown in table 5 to prove that iPIX has better performances than the CARTOGAM system.

Table 5. Comparison between CARTOGAM and iPIX in terms of Minimum localization time (considering data collection only).

	^{137}Cs (100 nSv/h)	^{60}Co (1.0 μSv/h)
CARTOGAM	240 sec	480 sec
iPIX	120 sec	140 sec

The above tests have been repeated (see figures 29 and 30) but selecting one of the two own sources (^{137}Cs or ^{60}Co) of the CANBERRA small irradiator to simulate a background dose rate of ~2 μSv/h at the measurement point. Under such circumstances, iPIX was still able to localize a 412 kBq ^{241}Am point source independently of the coded-aperture mask used. In addition, the quality of the superimposed pictures was quite comparable to the ones obtained under natural background radiation (0.1–0.2 μSv/h). Nevertheless, iPIX fails in localizing the 226 kBq ^{60}Co and 368 kBq ^{137}Cs point sources when the background dose rate at the measurement was increased to ~2 μSv/h.

Further experiments with a similar configuration were performed, but placing this time the portable ^{241}Am source (see section 2.3) in front of iPIX. The source-to-detector distance was 330 cm in order to provide an ambient dose equivalent rate of ~1 μSv/h at the measurement point. The following steps were sequentially applied:

- CANBERRA small irradiator entirely shielded.
- Selecting the ^{60}Co source of the CANBERRA small irradiator to provide a background dose rate of ~215 μSv/h at the measurement point.
- Selecting the ^{137}Cs source of the CANBERRA small irradiator to provide a background dose rate of ~310 μSv/h at the measurement point.

The shutter-time was automatically fixed by iPIX to 1 sec and up to 200 frames were taken. The results obtained are presented in figures 31–33. Except for the mask R13e2, the two enhanced background radiation levels have caused a minimal impact to localize the portable ^{241}Am radioactive source.

3.7 Off-axis response

The evaluation of the iPIX off-axis response was carried out by means of the CANBERRA big irradiator. The iPIX gamma camera was firstly oriented so that the corresponding hotspot was visualized exactly at the center of its field-of-view. Thereafter, only its pan (horizontal) angle was varied sequently between −25° to +25° in steps of 5° while keeping its tilt (vertical) position fixed

2016 JINST 11 P08012

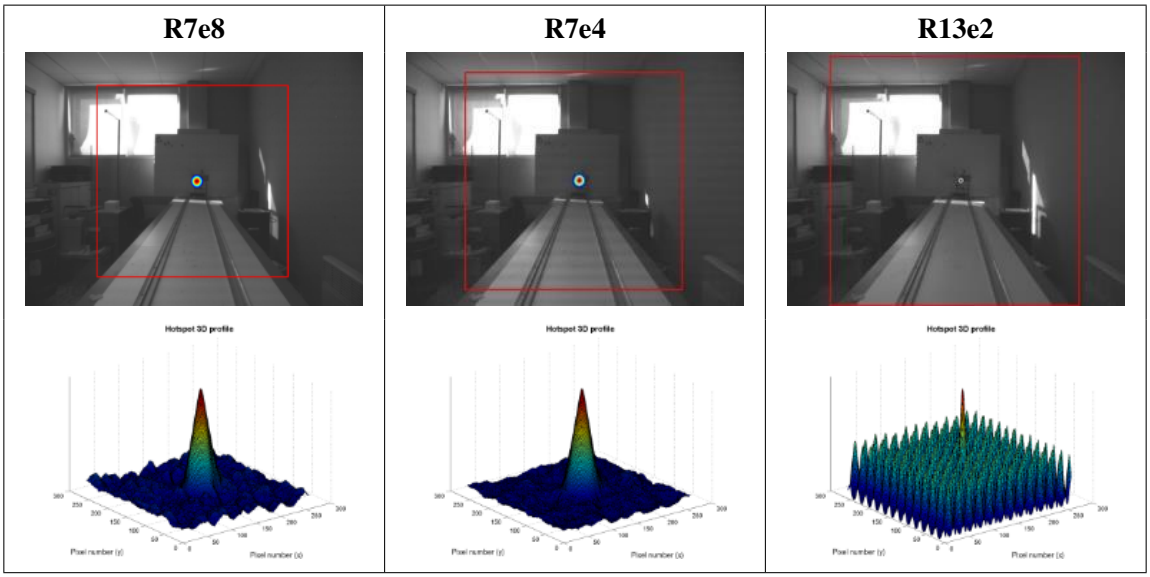

Figure 31. Results obtained for the 1.85 GBq ^{137}Am source located at a distance of 330 cm to the iPIX with natural background radiation condition (0.1–0.2 μSv/h).

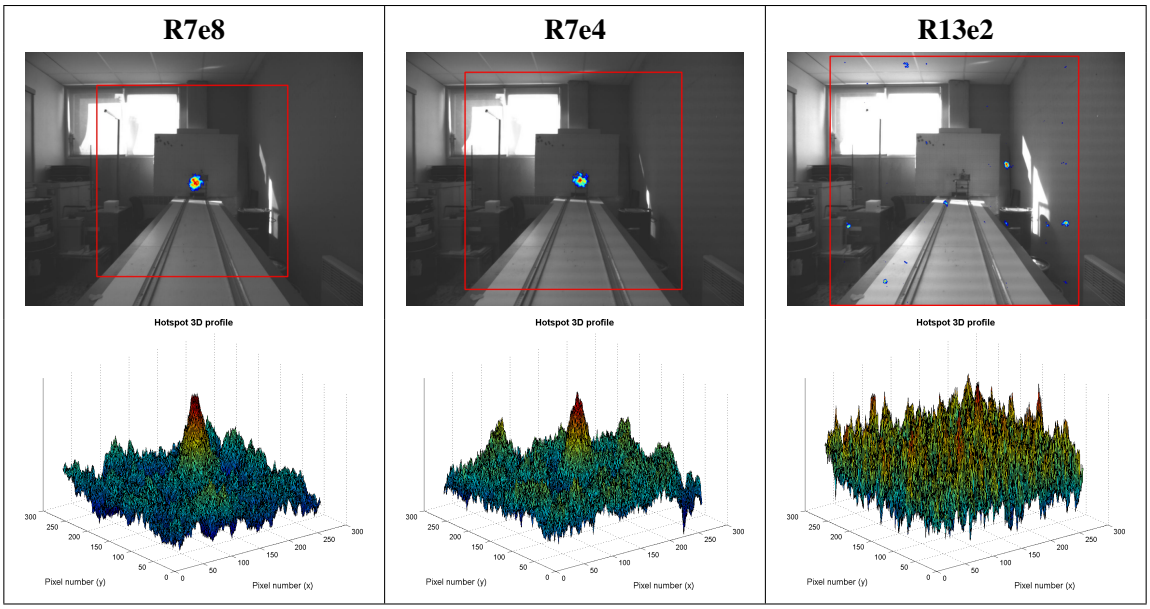

Figure 32. Results obtained for the 1.85 GBq ^{137}Am source located at a distance of 330 cm to the iPIX with an enhanced background dose rate of ~310 μSv/h generated by the ^{137}Cs source of the CANBERRA small irradiator.

to 0°, and *vice versa*. The measurements were performed using the masks R7e4 and R7e8. The −25° to +25° variation was considered to include the whole iPIX field-of-view.

The observed loss in counts for each mask was very similar with respect to both pan and tilt rotation angles. Figure 34 shows the average count rates, normalized to normal incidence (Pan = Tilt = 0°), measured with these two masks at varied pan or tilt rotation angle. The response deviation from an ideal behaviour (i.e., following the cosine function represented by a red dashed curve in

2016 JINST 11 P08012

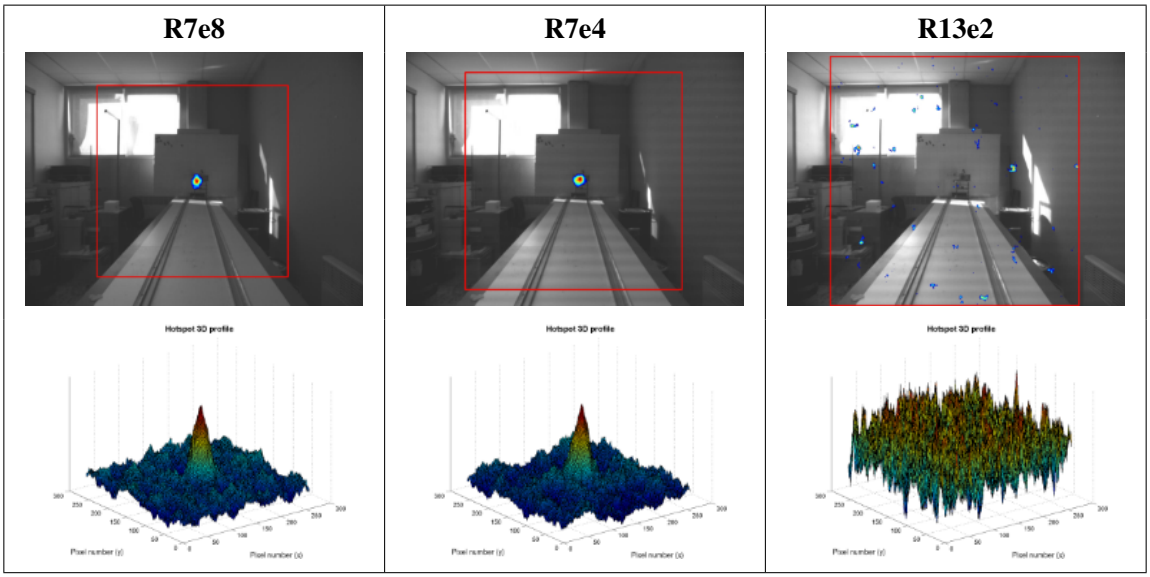

Figure 33. Results obtained for the 1.85 GBq ^{137}Am source located at a distance of 330 cm to the iPIX with an enhanced background dose rate of ~215 μSv/h generated by the ^{60}Co source of the CANBERRA small irradiator.

figure 34) is within 3%–12% for the mask R7e4 and never exceeds the limit of 25% for the mask R7e8. These deviations, which can be considered as negligible from the perspective of radiation dosimetry, are mainly due to the collimation effect of incident photons at the same coded-aperture mask. Admittedly, as illustrated in figure 35, the number of transmitted photons is decreased under non-normal incidences and thicker masks affecting moreover the shape of the projected open holes (they become oval instead of round) at the detector surface.

Nevertheless, as proved with a preliminary proof-of-concept prototype of iPIX [8], the self-attenuation effect is even more accentuated at low-energy photons (^{241}Am like sources) and the corresponding decrease in the iPIX response may surpass 50% for both the mask R13e2 and R7e4 (or even 80% for the mask R7e8) when the non-normal incidence is above 10°.

Concerning hotspot visualization, figure 36 displays an example of the superimposed pictures obtained at varied pan angles. According to this figure, a mirroring effect (i.e., false hotspot localization on the opposite side) may occur at the limit of the iPIX field-of-view (±25°). As illustrated in figure 37, this misleading artifact is caused by the projection on the detector surface of identical portions of the mask pattern. Therefore, it is suggested to systemically repeat any measurement resulting in a peripheral radioactive hotspot until this last is being targeted more directly. This will also have the benefit of increasing measurement statistics by mitigating the mask self-collimation effect.

3.8 Angular resolution

An important requirement in gamma imaging is the ability to track several radioactive sources at the same time. The angular resolution, θ, is the most convenient parameter to define the distinction limit between two small and adjacent radioactive sources. Theoretically, it depends on the diameter, d, of the open holes on the coded-aperture mask used and the distance, D, between the outer surface

2016 JINST 11 P08012

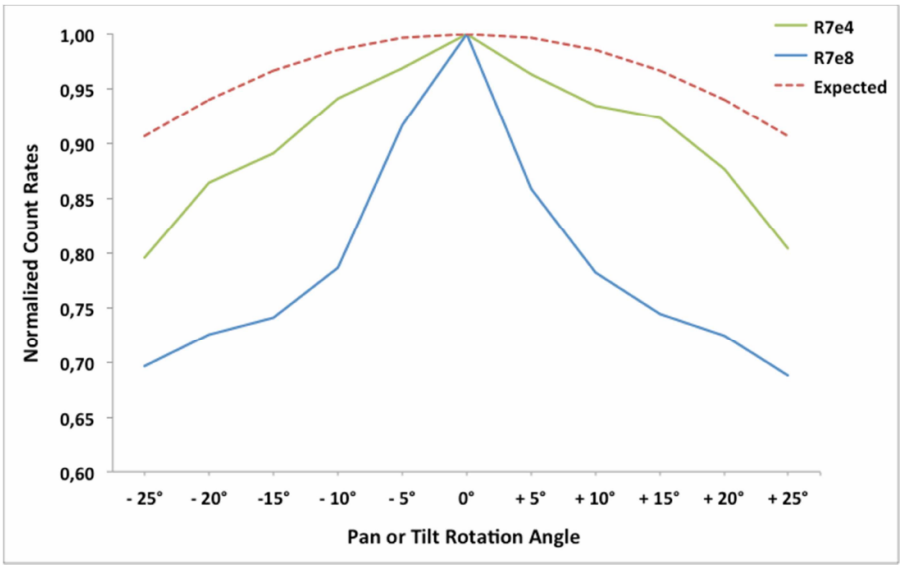

Figure 34. Normalized count rates observed for the masks R7e4 and R7e8 at varied pan or tilt rotation angles obtained with the ^{137}Cs source.

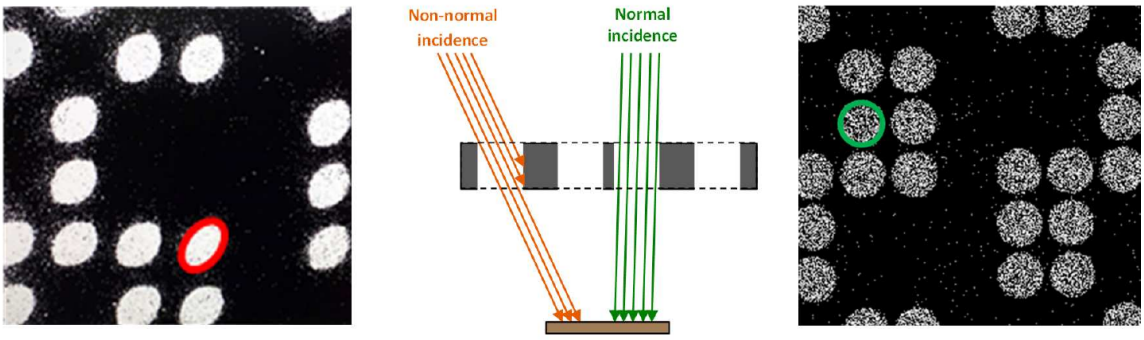

Figure 35. Mask self-collimation effect.

of this mask and the Timepix detector, as follows:

$$\theta_{\text{calculated}} = \tan^{-1}\left(\frac{d}{D}\right). \tag{3.1}$$

As illustrated in figure 38, the angular resolution can also be experimentally estimated from the vertical or horizontal axial profile of the hotspot peak, taking into account the associated FWHM (Full With at Half Maximum). Since the iPIX field-of-view (FOV) has a square shape, its side corresponds to the maximum number of available pixels (i.e., 256) on the considered axis and we can write then:

$$\theta_{\text{measured}} = \frac{\text{FOV} \times \text{FWHM}}{256}. \tag{3.2}$$

The theoretical and experimental angular resolutions for the three iPIX masks are summarized in table 6. According to this table, the experimental values obtained with the three masks agree to within 68% ($\pm$ 1σ) confidence level of their associated uncertainties with the theoretical ones. They also confirm that the angular resolution does not depend on the incident photon energy.

2016 JINST 11 P08012

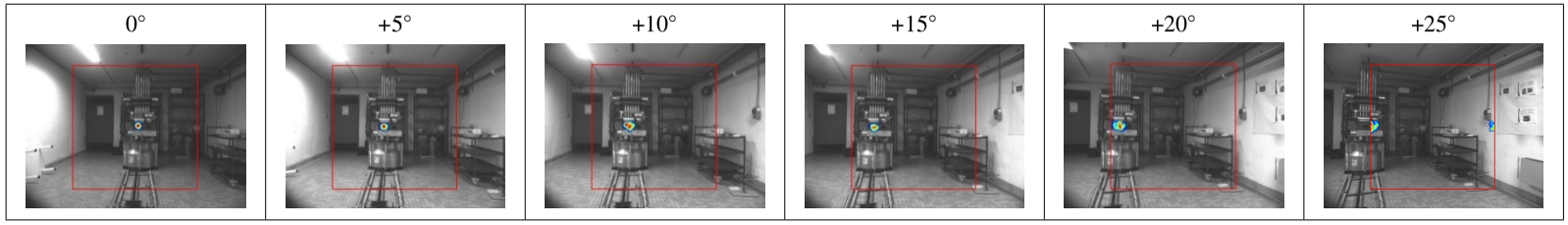

Figure 36. iPIX results at varied pan angles.

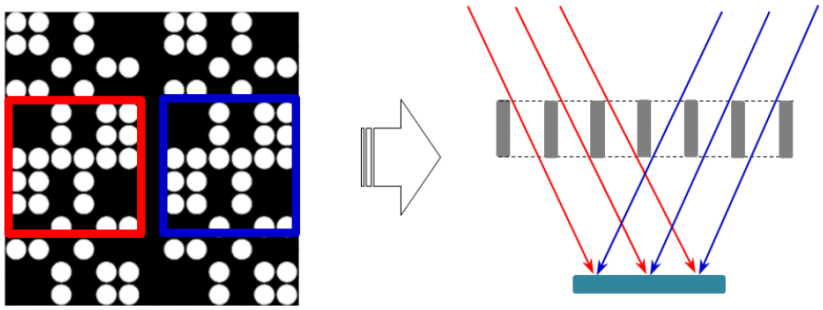

Figure 37. Illustration of the mirroring effect at the limit of the iPIX field-of-view. Radiation of the two peripheral sources (radiation direction indicated with red and blue arrows) project identical portions of the mask pattern on the detector surface.

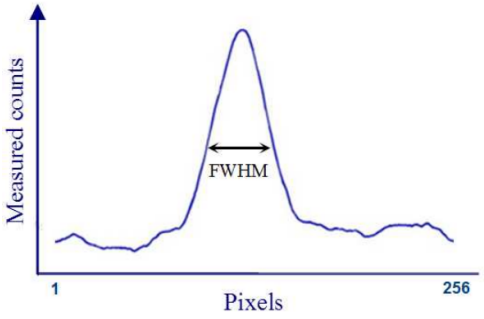

Figure 38. Vertical or horizontal axial profile the hotspot peak.

Table 6. Determination of the iPIX angular resolution.

		θ_{measured}		
	$\theta_{\text{calculated}}$	^{241}Am	^{137}Cs	^{60}Co
R13e2	2.5°	2.8° ± 0.6°	—	—
R7e4	6.0°	6.2° ± 0.6°	6.0° ± 0.6°	5.9° ± 0.6°
R7e8	5.0°	—	5.6° ± 0.7°	5.4° ± 0.7°

To illustrate the optimal angular resolution of iPIX when compared to the existing gamma imagers [5, 21], additional measurements were also carried out using three identical low-activity ^{241}Am point sources (340 kBq). These sources were placed on a horizontal line at 40 cm distance (i.e., providing 3 × 12 nSv/h dose rates at the measurement point). As summarized in figure 39, the following experimental configurations were considered:

a. All the sources were close to each other but the outside sources have remained separated from the central one by ∼4 cm, which is the diameter of their circular support. This represents around ±6° separation angle.

b. The outside sources were separated by ±5 cm (i.e., ±7°) from the central source.

c. The outside sources were separated by ±10 cm (i.e., ±14°) from the central source.

2016 JINST 11 P08012

Satisfying results were obtained with the masks R7e4 and R7e8 (see figure 39 and figure 40, respectively). However, it is not possible to determine the exact location of each one of the three sources when they are very close to each other (i.e., ±6° separation angle). In addition, the strong decrease of count rates at non-normal incidences corroborate the mask self-collimation effect, which has already been discussed in the previous section. Due to this effect, the outside sources are less visible at ±14° separation angle.

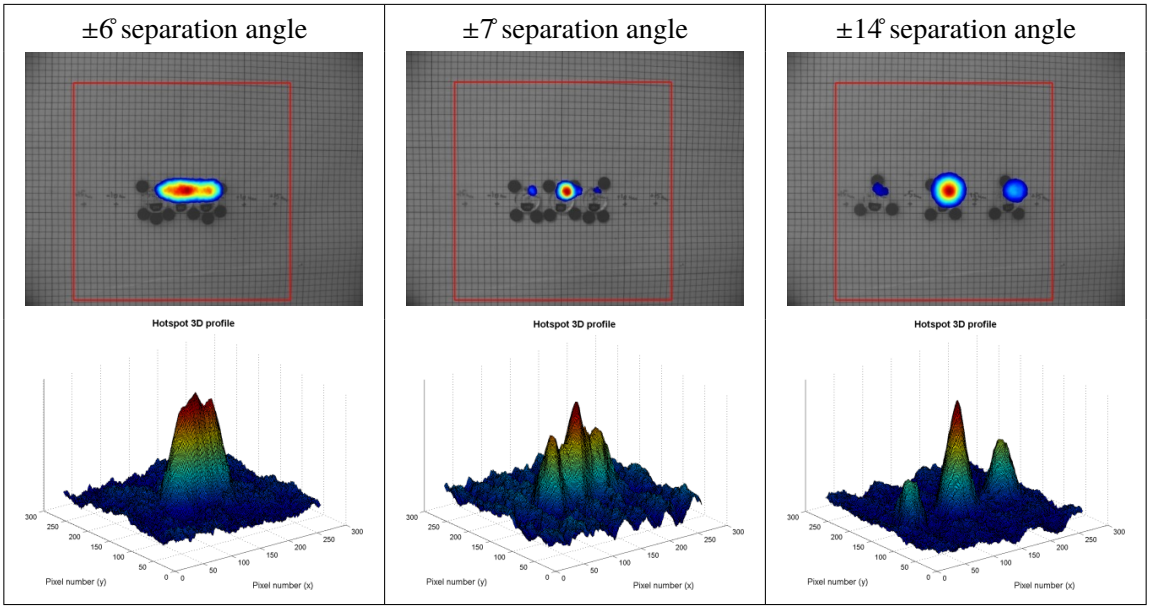

Figure 39. Measurement results of three identical ^{241}Am sources with mask R7e4 at different separation angles.

4 Conclusions

We have carried out a comprehensive experimental characterization of the iPIX gamma imager to explore its main features and performances. In view of all the results obtained with ISO narrow X-ray beams at varied acceleration voltages and currents, we have observed that the Timepix shutter-time is the most critical parameter for an effective localization of radioactive hotspots and must be conveniently chosen to avoid signal distortions on the Timepix detector due to pulse pile-up and/or summation effects.

Compared to existing gamma imagers, iPIX has an enhanced angular resolution (between 2.5° and 6.0°, depending on the coded-aperture mask used) and a high response sensitivity at low energies, tolerating at the same time high levels of background radiation (around 200–310 μSv/h).

Regarding its localization capability, an ^{241}Am source providing only 2 nSv/h dose rate at the measurement point was clearly spotted within 70 sec of data collection time. In the same way, iPIX was able to localize low-activity ^{137}Cs and ^{60}Co sources (providing 100 nSv/h and 1 μSv/h dose rates at the measurement point, respectively) with less than 2.5 min of data collection time.

This study has demonstrated that the mask R7e8 can be applied to almost the whole energy range of interest (10 keV–1.5 MeV). Whereas mask R13e2 is limited to only low photon energies

2016 JINST 11 P08012

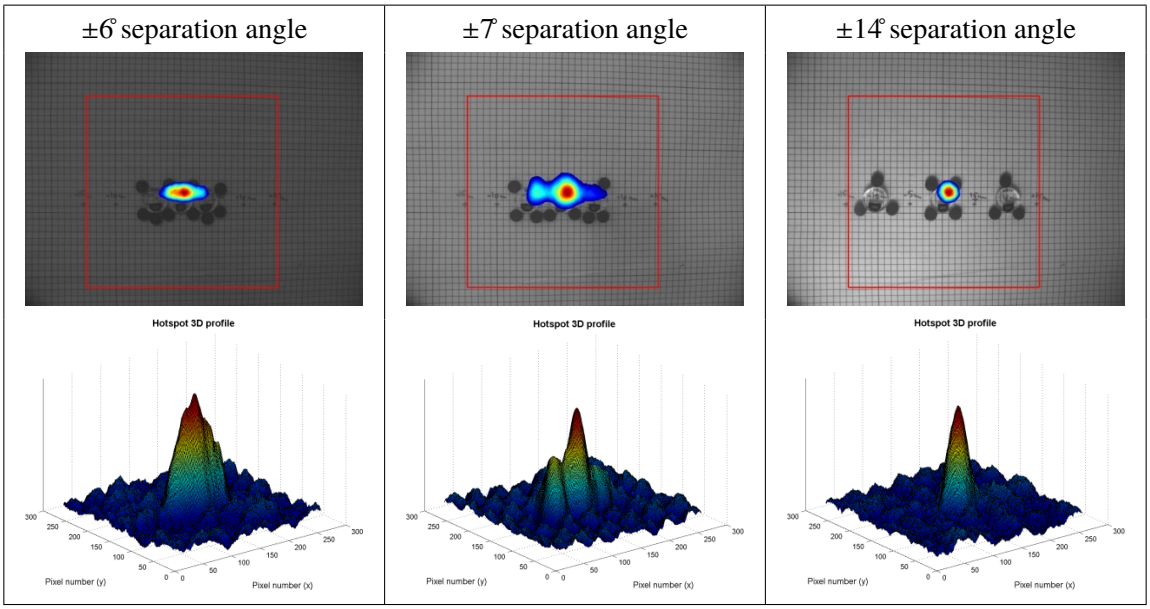

Figure 40. Measurement results of three identical ^{241}Am sources with mask R7e8 at different separation angles.

(e.g. 59 keV γ-rays of ^{241}Am, whose detection usually indicates the presence of plutonium in nuclear wastes). As an intermediate application, mask R7e4 is able to localize radioactive sources in the medium photon energy range of ^{137}Cs.

Finally, the iPIX dose rate response curve was equally checked with several standard ^{137}Cs sources of different activities showing a quite linear behaviour over a wide range covering nearly 8 decades (10^{-6}–10^{1} Sv/h).

Acknowledgments

This study has been partially funded by the European Union Seventh Framework Programme, Marie Curie Actions, through the EDUSAFE Initial Training Network (EU FP7-PEOPLE-2012-ITN-316919). The authors would also like to acknowledge the staff of both CANBERRA and KIT (in particular T. Liedtke for providing figure 10) irradiation facilities for their valuable technical support.

References

[1] International Atomic Energy Agency, *Combating illicit trafficking in nuclear and other radioactive material. Reference manual*, IAEA Nuclear Security Series No. 6, IAEA, Vienna Austria (2007).

[2] Nuclear Energy Agency, *Strategic aspects of nuclear radiological emergency management. Planning for Effective Decision Making. Consequence Management and Transition to Recovery*, NEA No. 6387, OECD (2010).

[3] V. Schoepff et al., *BOOSTER: Development of a Toolbox for Triage of a Large Groups of Individuals Exposed to Radioactive Material*, *IEEE Trans. Nucl. Sci.* **61** (2014) 2210.

2016 JINST 11 P08012

[4] H.O. Anger, *Use of a gamma-ray pinhole camera for in vivo studies*, *Nature* **170** (1952) 200.

[5] O. Gal et al., *CARTOGAM — a portable gamma camera for remote localization of radioactive sources in nuclear facilities*, *Nucl. Instrum. Meth.* **A 460**(2001) 138.

[6] O. Gal et al., *Development of a portable gamma camera with coded aperture*, *Nucl. Instrum. Meth.* **A 565** (2006) 233.

[7] M. Gmar et al., *GAMPIX: a new generation of gamma camera*, *Nucl. Instrum. Meth.* **A 652** (2011) 638.

[8] K. Amgarou et al., *Evaluation of the next generation gamma imager*, in proceedings of the *3rd International Conference on Advancements in Nuclear Instrumentation Measurement Methods and their Applications (ANIMMA 2013)*, Marseille, France, June 23–27 (2013), IEEE (2013).

[9] X. Llopart, R. Ballabriga, M. Campbell, L. Tlustos and W. Wong, *Timepix, a* 65*k programmable pixel readout chip for arrival time, energy and/or photon counting measurements*, *Nucl. Instrum. Meth.* **A 581** (2007) 485.

[10] R.H. Dicke, *Scatter-Hole Cameras for X-Rays and Gamma Rays*, *J. Astrophys.* **153** (1968) L101.

[11] G. Vedrenne and J.-L. Atteia, *Gamma-Ray Bursts. The brightest explosions in the Universe*, Springer-Verlag Berlin Heidelberg and Praxis Books (2009).

[12] J. Braga et al., *A new mask-antimask coded-aperture telescope for hard X-ray astronomy*, *Exp. Astron.* **2** (1991) 101.

[13] International Organization for Standardization, *X and gamma reference radiation for calibrating dosemeters and doserate meters and for determining their response as a function of photon energy — Part 4: Calibration of area and personal dosemeters in low energy X reference radiation fields*, ISO/CD 4037-4 (2004).

[14] D. Turecek, T. Holy, J. Jakubek, S. Pospisil and Z. Vykydal, *Pixelman: a multi-platform data acquisition and processing software package for Medipix2, Timepix and Medipix3 detectors*, 2011 *JINST* **6** C01046.

[15] K. Akiba et al., *The Timepix Telescope for High Performance Particle Tracking*, *Nucl. Instrum. Meth.* **A 723** (2013) 47 [arXiv:1304.5175].

[16] C. Teyssier et al., *Performance of the Medipix and Timepix devices for the recognition of electron-gamma radiation fields*, *Nucl. Instrum. Meth.* **A 650** (2011) 92.

[17] J. Jakubek et al., *Spectrometric properties of TimePix pixel detector for X-ray color and phase sensitive radiography*, *IEEE Nucl. Sci. Symp. Conf. Rec. (NSS/MIC)* (2007) 2323.

[18] E.E. Fenimore and T.M. Cannon, *Coded aperture imaging with uniformly redundant arrays*, *Appl. Opt.* **17** (1978) 337.

[19] S.R. Gottesman and E.E. Fenimore, *New family of binary arrays for coded aperture imaging*, *Appl. Opt.* **28** (1989) 4344.

[20] ICRP, *Conversion coefficients for use in radiological protection against external radiation*, ICRP Publication 74, *Ann. ICRP* **26** (1996) 1 [*Erratum ibid.* **27** (1997) 1].

[21] C.G. Wahl et al., *The Polaris-H imaging spectrometer*, *Nucl. Instrum. Meth.* **A 784** (2015) 377.

2016 JINST 11 P08012